TU Delft

Master Thesis Report

Biomimicry: Natural topographies to control cell behaviour

Floris Honig

4295692

August 2018

Supervisors: Steven Vermeulen

Jan de Boer

Lidy Fratila-Apachitei

Amir Zadpoor

Lab: cBITE, Cell Biology-Inspired Tissue Engineering

Institute: MERLN institute for Technology-Inspired Tissue Engineering

Maastricht University

MERLN Institute

Abstract

The use of material properties to guide cell behaviour is often utilised in the field of regenerative medicine. Regarding this, surface topography has been shown to control different cellular processes. In nature, topographies exist in a wide variety of shapes, including hierarchical structures with a great degree of surface roughness. Here, inspired by nature, the potential of such surface characteristics in guiding cell behaviour was investigated via replication of 32 natural surfaces onto polystyrene using hot embossing techniques. Fluorescent image analysis of bone marrow-derived human mesenchymal stem cells cultured on these surfaces showed that cell shape was greatly affected by the distinct topographical features compared to a flat surface. Cluster analysis identified groups showing similar effect on nuclear and cell morphological parameter such as size, orientation and compactness. Related to this, focal adhesion formation and organisation was highly dependent on surface topography. Namely, focal adhesion maturation was promoted on the natural topographies. Furthermore, mouse embryonic stem cell pluripotency and colony morphology was influenced by natural topographies. Finally, natural topographies modulated *in vitro* mesenchymal stem cell differentiation. This study shows the capability of natural topographies to regulate cell behaviour useful for regenerative applications.

Introduction

The field of regenerative medicine aims to develop novel therapies for the replacement or regeneration of damaged tissues and organs in order to restore normal function. To achieve this, stem cells are often utilised because of their self-renewal capability and differentiation potential into other types of cells[1]. The potential of various types of stem cells are being studied, including embryonic stem cells (ESCs) and mesenchymal stem cells (MSCs). ESCs are pluripotent cells derived from the inner cell mass, capable of giving rise to more than 200 types of cells of the three embryonic germ layers[2]. MSCs however, are multipotent cells that have the ability to turn into a variety of adult cell types developing mainly from the mesoderm and can be obtained from several adult tissues such as the bone marrow[3]. Currently approved regenerative therapies employ different strategies to control the behaviour of these cells[4]. For example, conventional methods include the addition of biochemical supplements such as growth factors to regulate cell differentiation[5]. Other approaches involve the use of materials as a tool to provide signals to direct cell fate. The cell-material interface thereby forms a dynamic environment in which the material guides cell behaviour through its inherent properties[6]. Cells are known to respond to the chemistry, mechanics, structure and degradability of a material[7]. Concerning this, surface topography, which describes the shapes and features of an area, is recognised to control cell behaviour, including cell adhesion, proliferation and differentiation[8–10]. Therefore, topographical design of biomaterials is a powerful approach to influence the interaction between cells and biomaterials, both relevant to enhance *in vitro* cell culture systems and to improve biocompatibility and integration of medical devices.

Topographies exist in different sizes and shapes both at the micro- and nanoscale, leading to diverse cell responses. For instance, nanotopographies have been used to stimulate osteogenic differentiation in human mesenchymal stem cells (hMSCs)[10]. In addition, microtopographies can regulate stem cell lineage commitment by affecting cell shape and adhesion[9]. However, the underlying mechanisms defining the interplay between topography and cell phenotype remain complex. This makes it difficult to find the optimal surface topography for a given application. Previously, to address this problem, high-throughput systems have been used to identify surface topographies that generate a specific cell response[11–13]. For example, the TopoChip[11] platform found topographies supporting pluripotent maintenance of induced pluripotent stem cells (iPSCs) through simultaneous screening of more than 2000 randomly generated topographical features based on mathematical algorithms using shapes of circles, triangles and rectangles[14]. Similarly, other high-throughput platforms, such as the BSSA[12] and MARC[13] systems, identified topographies that influence fibroblast growth[15] and enhance differentiation of neural progenitor cells into neurons[16]. Although these miniaturised platforms offer a great tool to identify the most optimal surface topographies that induce specific cell behaviour *in*

vitro, there are technological and design limitations. They often focus on a restricted area of the biomaterial design space, thereby omitting other parameters known to steer cell behaviour. For example, topographical design of the TopoChip[11] only varies feature size, shape and spacing of the distinct topographies, while keeping the height constant. Consequently, surface roughness is not controlled, topographies show no hierarchical structures and lack disorder, while these properties are known to steer cell behaviour *in vitro.* For instance, hierarchical structures have shown to support proliferation and differentiation compared to flat substrates of distinct types of cells[17,18]. In addition, it has been demonstrated that surface roughness plays an important role in regulating cell adhesion, morphology and differentiation[19–21]. Moreover, nanoscale disorder has proven to stimulate cell differentiation[10]. High-throughput systems only vary a limited number of parameters of the total design space of the substrate.

Over the years of evolution, nature has developed numerous biological materials with unique surface structures optimised to serve different functions. For instance, nanostructures on cicada wings limit bacterial attachment through mechanical rupture[22], the holy lotus (*Nelumbo Nucifera)* has superhydrophobic leaves for self-cleaning purposes based on hierarchical surface structures[23] and denticle structures aligned in the direction of the flow on a shark's skin reduce friction drag[24]. Moreover, natural topographies exist in a wide variety of shapes[25,26], show a high degree of surface roughness and possess dual-scale structures both at the micro- and nanoscale. As mentioned before, these properties are of great importance to control cell behaviour on artificial surfaces *in vitro*. Interestingly, only a few studies have employed natural topographies in biomimetic design to control cell behaviour. For instance, the prismatic topography of a mollusc shell (*Pinctada maxima)* induces MSCs to undergo osteogenesis[27], titania nanowire arrays inspired by the cicada wing can eliminate bacteria while guiding mammalian cell adhesion and proliferation[28] and superhydrophobic lotus-like structured films prevent platelet adhesion which is useful to impede coagulation[29]. Thus, natural topographies can be utilised for bioinspired design of artificial biomaterials to regulate cell behaviour.

In this study, a bioinspired approach is taken to identify natural topographies that induce novel cell responses, which will provide new insights into the relationship between surface topography and cell phenotype. A total of 32 natural surfaces, including plant leaves and insect wings, selected based on variety in surface architecture were imprinted into polystyrene (PS) surfaces using hot embossing. Subsequently, the effect of these topographies on the behaviour of bone marrow-derived hMSCs and mouse ESCs was examined. This study pioneers in simultaneously investigating the potential of several natural topographies in the development and fabrication of a new line of artificial surfaces for regenerative applications.

Materials & Methods

Replication of natural surfaces

Replication of natural surfaces was achieved by a two-step fabrication process using soft lithography and hot embossing inspired by Goral *et al.*[30]. The first step included the fabrication of a polydimethylsiloxane (PDMS) mould, which contains the negative imprint of the natural surface (Fig. 1A, top). A sample of the fresh natural surface of choice (e.g. rose petal) was fixed onto a petri dish using double-sided adhesive tape made of foam with synthetic rubber (Double Fix, Bison). After, the silicon resin and curing agent (Sylgard® 184 Elastomer Kit, Dow Corning) were mixed with a ratio of 10:1 (w/w) and cast onto the natural surface. Subsequently, the liquid mixture was degassed and cured for 48 hours (hrs) at room temperature to prevent heat damage by going above the melting points of the epicuticular wax structures of natural surfaces[31]. Finally, the solid PDMS mould was separated from the natural surface without any adhesion of natural material to the PDMS (Supp. Fig. 1). In the second step, the PDMS mould was used to imprint the positive surface structure into PS using hot embossing (Fig. 1A, bottom). To achieve this, an assembly was made in which a 190µm thick PS film was placed on the PDMS mould clamped between two Teflon sheets and microscope slides to apply constant pressure (Supp. Fig. 2). Then, glass-transition of the PS film (T_g: 95^{o}C) was achieved by putting the entire system inside an oven for 1hr at 150^{o}C (PDMS is stable up to 200^{o}C). After, the assembly was removed from the oven and cooled down to room temperature to allow the PS film to solidify. Finally, the PS surface with copied surface topography was carefully peeled off the PDMS mould.

Scanning electron microscopy (SEM)

Scanning electron microscopy was used for examination of the surface topography of natural surfaces and for quality control of their respective PS replicas. Preparation of fresh natural samples consisted of fixation with 2% glutaraldehyde in 0.1M cacodylate buffer for 1hr. Subsequently, the samples were washed three times in 0.1M cacodylate before dehydration by immersion in a graduated series of ethanol in water (50%, 70%, 90%, 100%). Then, samples were critical point dried (EM CPD300, Leica) using 15 exchange cycles with slow gas out and heating speed settings. All samples were mounted on SEM stubs using carbon conductive adhesive tape. Finally, samples were sputter-coated with gold (Sputter Coater 108auto, Cressington) for 100 seconds prior to imaging using a scanning electron microscope (XL-30, Philips) at 10kV.

Profilometry analysis

For surface shape characterisation, the natural surfaces and PS replicas were investigated using profilometry. A 3D laser confocal scanning microscope (VK-X Series, Keyence) was deployed to image

all samples at different magnifications. Visualisation and analysis of the data was performed with VK-X Series Software (Keyence). Measurements to compute the mean surface roughness were taken along multiple lines (n=6) across the surface including tilt correction. Anisotropic surface structures were measured in the same direction for both natural surface and replica.

Cell culture

Bone marrow-derived human mesenchymal stem cells (BM-hMSCs) were isolated and expanded from bone marrow provided by the orthopaedic department of the Maastricht University Medical Center+. Basic medium for BM-hMSCs consisted of MEM Alpha GlutaMAXTM (Gibco), 10% v/v foetal bovine serum (FBS), 0.2mM ascorbic-acid-2-phosphate (ASAP), 10 U/mL Penicillin/Streptomycin. Cells were grown at 37°C in a humid atmosphere at 5% CO2. Upon reaching confluence, cells were seeded on topographies and flat control at a cell density of 5000 cells/cm^2 for experimental use. BM-hMSCs of passage 3 and 4 were used.

Mouse embryonic stem cells (mESCs) were cultured on a fibroblast feeder layer in Dulbecco's modified Eagle's medium (DMEM, Sigma-Aldrich), including 2% GlutaMAX, 10% FBS, 1% non-essential amino acids. 1% HEPES, 50µm mercaptoethanol and 1% Leukemia inhibitory factor (LIF). Medium was refreshed every two days and cells were trypsinised every three days. Cells were seeded on PS surfaces at a cell density of 10000 cells/cm^2. If required, surfaces were coated with in 0.15% gelatin (Sigma-Aldrich) for 30 min at 37°C before addition of cells.

Immunocytochemistry

For visualisation of nuclear and cell shape a CellPaint assay designed by the Broad Institute of Harvard and MIT was used[32]. Before fixation, mitotracker deep red (Invitrogen) was added to the medium in a final concentration of 500nM for 30 minutes (min). Subsequently, samples were washed with Hank's balanced salt solution (HBSS, ThermoFisher) and fixed in 3.6% formaldehyde (VWR) for 20 min at room temperature (RT). Then, permeabilization was achieved by addition of 0.1% Triton-X-100 in HBSS for 10 min. Cells were washed twice with HBSS and incubated for 30 min at RT in a staining solution composed of: 5µg/mL wheat germ agglutinin 584 (Invitrogen), 10µM SYTO 14 green fluorescent nucleic acid stain (Invitrogen), 50µg/mL concanavalin 488 (Invitrogen), Phalloidin 568 (ThermoFisher) diluted 1:80 and Hoechst (ThermoFisher) diluted 1:1000. After, cells were washed three times and mounted on microscope slide using mounting medium (Dako, Agilent technologies). The cover slips were sealed using nail polish and put to dry overnight at RT. The next day, microscope slides were put in the dark at 4°C. At this point, samples were ready to be used for imaging.

The staining protocol for phosphorylated focal adhesion kinase (pFAK) and Oct4 differed from the CellPaint assay. Cells were washed with phosphate buffered saline (PBS, Sigma-Aldrich) before fixation

in 3.6% formaldehyde for 10 min at 37°C. After, cells were washed three times with PBS and permeabilised by addition of 0.1% Triton-X-100 in PBS for 10 min. Following this, samples were blocked using serum (1:100) in PBT (0.02% Triton-X-100, PBS & 0.6% bovine serum albumin) for 1hr. Subsequently, samples were incubated in primary antibodies diluted in PBT for 1hr. Primary bodies used in experiments include: anti-FAK (phosphor Y397) (1:400, abcam) and Oct3-/4 antibody (3µg/mL, R&D Systems). After another washing step samples were incubated in secondary antibody Alexa Fluor™ (1:500, ThermoFisher) with desired targets. Finally, Hoechst (1:1000, ThermoFisher) was used for visualisation of nuclei. For mESCs the membrane was stained using CellMask™ orange (1:3000, ThermoFisher). All steps were done at room temperature. Mounting procedure used was same as previously described.

Adipogenic differentiation

BM-hMSCs were seeded at a density of 15000 cells/cm^2 on distinct natural topographies and flat controls. After 24hrs, basic medium was changed to adipogenic differentiation medium and control medium and refreshed every second day. Adipogenic differentiation medium consisted of DMEM (Gibco), 10 U/mL Penicillin/Streptomycin, 10% FBS, 0.2mM indomethacin (Sigma), 0.5mM IBMX (Sigma), 1µM dexamethasone (Sigma) and 10µg/mL Insulin (human, Sigma), while control medium consisted of DMEM (Gibco) and 10% FBS. After 21 days, cells were fixed in 3.6% formaldehyde (VWR) including 1% $CaCl_2.2H_2O$ (Merck) for 4hrs. Subsequently, cells were rinsed with MilliQ and incubated in 60% 2-propanol (VWR) for 5 min. Then, to visualise fat formation, cells were stained with 0.3% (w/v) Oil Red O solution (Sigma) for 5 min and washed with MilliQ. Finally, nuclei were visualised using Hoechst (1:1000, ThermoFischer).

Mineralisation experiment

BM-hMSCs were seeded at a density of 5000 cells/cm^2 on distinct natural topographies and flat controls. After 24hrs, basic medium was changed to mineralisation medium and control medium and refreshed every second day. Mineralisation medium consisted of MEM Alpha GlutaMAXTM (Gibco), 10% v/v foetal bovine serum (FBS), 0.2mM ascorbic-acid-2-phosphate (ASAP), 10 U/mL Penicillin/Streptomycin (Pen/Strep), 100nM dexamethasone (Sigma) and 10mM b-glycerol phosphate, while control medium included the same components except dexamethasone. After 35 days, cells were fixed in 3.6% formaldehyde for 4hrs and subsequently stained in 2% aqueous Alizarin red solution (pH=4.2) for 2 min. After, the excess stain was washed off with MilliQ. Lastly, nuclei were visualised using Hoechst (1:1000, ThermoFischer).

Image acquisition and data analysis

Mounted slides were imaged using a fluorescent microscope (Nikon Eclipse Ti) with a Plan Apo 20x objective (NA=0.75) and an Andor Zyla 5.5 camera (4MP). Efficient image analysis was performed in CellProfiler[32] software by building a robust pipeline for each experiment. Images were corrected for illumination using appropriate illumination functions followed by identification of nuclear and cellular morphological parameters. A description of these parameters can be found in Supplementary Table 4. ImageJ[33] was used to visualise fluorescent images and measure the feature diameter of natural topographies. Data analysis and graphics were performed in R[34] using the ggplot2 package. For cluster analysis, distance matrices were calculated in the Euclidean space from the scaled median morphological parameters. Hierarchical clustering was performed with the average linking method using the R package pvclust[35]. Results of Heatmap and principal component analysis were extracted and plot with aid of the R package Factoextra[36]. Statistical significance of the cellular and nuclear shape parameters was computed using a Tukey HSD test. Statistical significance of focal adhesion and adipogenic differentiation data between different surfaces was obtained using a pairwise t-test using Benjamini-Hochberg multiple testing correction. Significance levels of all tests included *$p<0.05$.

Results

Characterisation and quality control of natural surfaces and replicas

To visualise the specific topographical features of the selected natural surfaces and to check for the fidelity of the replicated PS surfaces, scanning electron microscopy was used. Among the 32 replicated surfaces a wide variety of topographies can be identified, which showed good resemblance to the original natural surfaces (Supp. Table 1). The replication method proved to successfully replicate different types of natural topographies both at the micro- and nanoscale (Fig. 1). For example, the hierarchical structures of the rice plant (*Oryza sativa*) and the holy lotus (*Nelumbo nucifera*) replicas matched their original topographies, even copying the epicuticular waxes. Furthermore, replicated nanostructures such as the cuticular folds on the micropapillae of the red rose (*Rosa)* and the nanopillars of the cicada (*Yanga adriana)* mimicked the authentic natural structures. Occasionally, small differences were observed between the original and replicated surfaces. For example, the grooves of the red rose replica are larger than the original surfaces. However, topographical dimensions were similar for both the replica and original surface, as evident from the similar diameters of the topographical features (e.g. papillae and nanopillars) of both types of surfaces (Supp. Fig. 3). Accurate topographical replication also led to functional replication of the natural surfaces. Namely, replicas of superhydrophobic plant leaves displayed similar contact angles as the original surface

(Supp. Table 3). Water droplets rolled-off both the replicated (Movie. 1) and original surface (Movie. 2). Overall, topographies of natural surfaces were replicated onto PS surfaces with great precision.

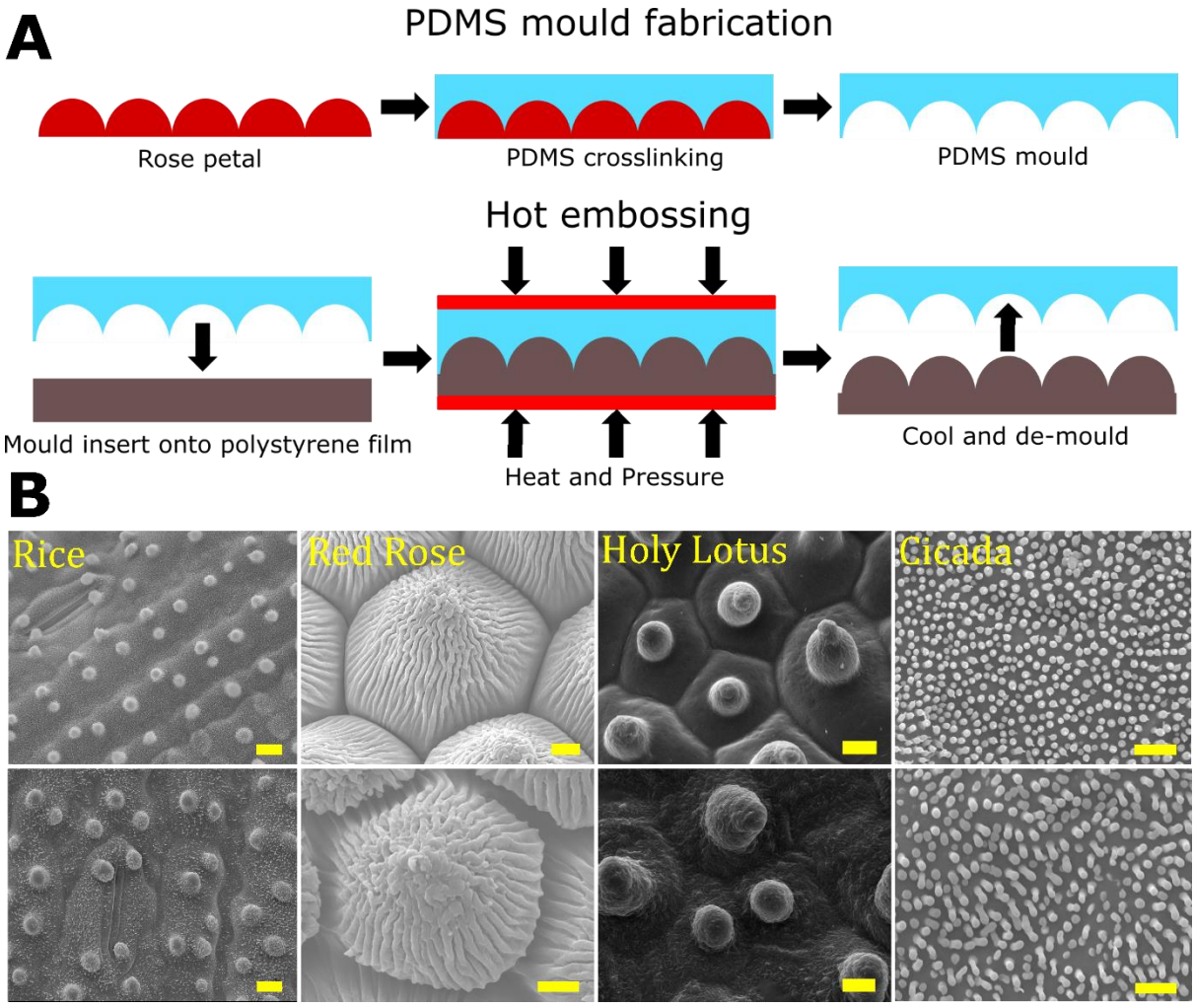

Figure 1. Replication method and SEM analysis of natural surfaces and their respective replicas. (A) Two-step fabrication scheme showing replication method of natural surfaces. First, a PDMS mould containing the negative imprint of the natural surface topography is fabricated **(top)**. After, this mould is used to imprint the surface structures into a PS film using hot embossing **(bottom)**. **(B)** Surface topography of the PS replicas **(bottom)** mimic their corresponding original natural surface **(top)**. The rice plant (*Oryza sativa*) topography is characterised by parallel ridges on which several micropapillae are displayed covered by nanowaxes. The red rose (*Rosa*) surface structure consists of micropapillae that exhibit cuticular folds. Epicuticular waxes together with larger micropapillae define the topography of the holy lotus (*Nelumbo nucifera*). Arrays of nanopillars describe the topography on the wing of the cicada (*Yanga adriana).* Scale bars: bottom right, 5µm.

Profilometry was used to gain insight into the height distribution of the replicated and original plant surfaces (Fig. 2A; Supp. Table 2). The distinct plant surfaces showed different degrees of surface roughness depending on their topographical features (Fig. 2B). For instance, small protrusions on the surface of the calla lily (*Zantedeschia*) resulted in a low degree of surface roughness and larger features such as the ridges of the onion (*Allium*) and the papillae of the red rose caused a higher degree of surface roughness (Fig. 2; Supp. Table 2). Moreover, original natural surfaces and their respective

replicas displayed comparable mean roughness values (Fig. 2B), which confirmed the quality of the PS replicas. The few replicas that showed statistically different mean roughness values than their original surface (e.g. rice) might be caused by the pressure applied during the hot embossing process. Altogether, a great diversity in inherent surface roughness can be identified among the different surfaces, with similar roughness for the original and replicated surfaces. Profilometry was not able to detect the nanofeatures of the original and replicated cicada surfaces.

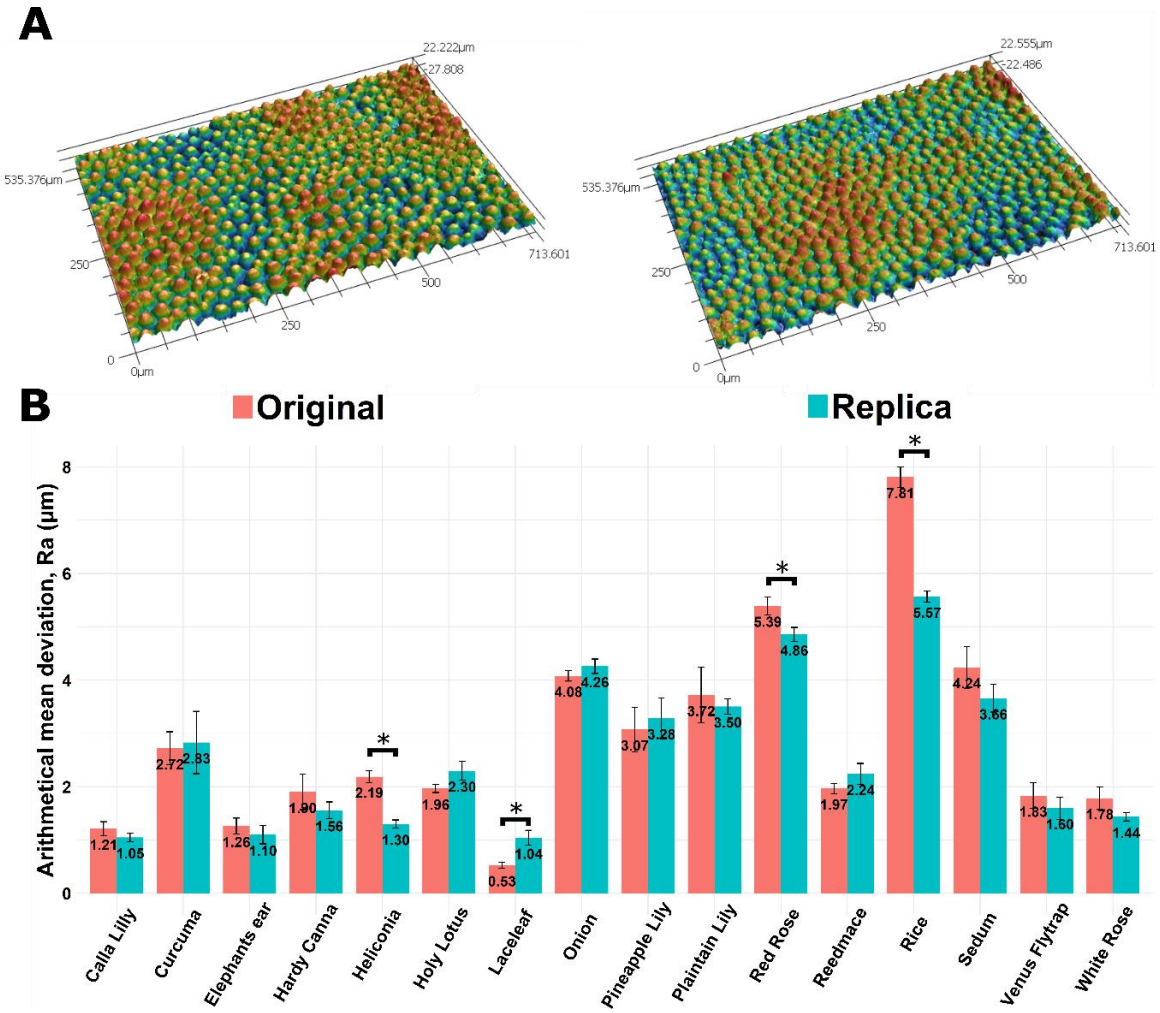

Figure 2. Profilometry analysis of plant surfaces and respective replicas showing different degrees of roughness. (A) 3D surface topography image of original **(left)** and replicated surface of the red rose (*Rosa*). **(B)** Bars represent the average arithmetical mean deviation values (Ra) of the original plant surfaces and replicas. Error bars denote standard error of the mean (n=6). Welch's t-test: *p<0.05.

Natural surface topographies control cellular and nuclear morphology

In literature, it is known that micro- and nanotopographies guide the morphology in various types of cells, which are often linked to other cellular processes such as differentiation[37–39]. To investigate the effect of natural topographies on cell morphology and size, BM-hMSCs were seeded on all PS replicas and a flat control surface. The cells were allowed to adapt to their environment for 24hrs. At this time

point, the cells were fixed and stained with Hoechst and Phalloidin to enable visualisation of cellular morphology. Natural topographies guided a large range of cell shapes between the distinct natural topographies, of which a selection is shown in Fig. 3. In absence of any topography, cells spread across different directions of the flat surface. On the contrary, hMSCs arranged around and on top of the micropapillae of the leaf structures. A different response was observed on the onion replica, where cells showed elongated anisotropic alignment along the ridges of the surface. Interestingly, a combination of these morphologies was seen on the hierarchical structure of the rice surface. For this surface, cells responded to the papillae while showing directional dependency. Furthermore, on the venus flytrap (*Dionaea muscipula*) replica, cells gathered around the gland structures of the surface. Cells on the protrusions of the calla lily and the nanopillars of the cicada orange (*Becquartina electa*) showed a compact shape. Moreover, varying cell sizes were observed among the different surfaces. For instance, similar cell size was observed on the venus flytrap, onion and flat surfaces, while the cells sizes on the rice and lotus surfaces were smaller. In short, natural topographies induced different cell shapes and sizes.

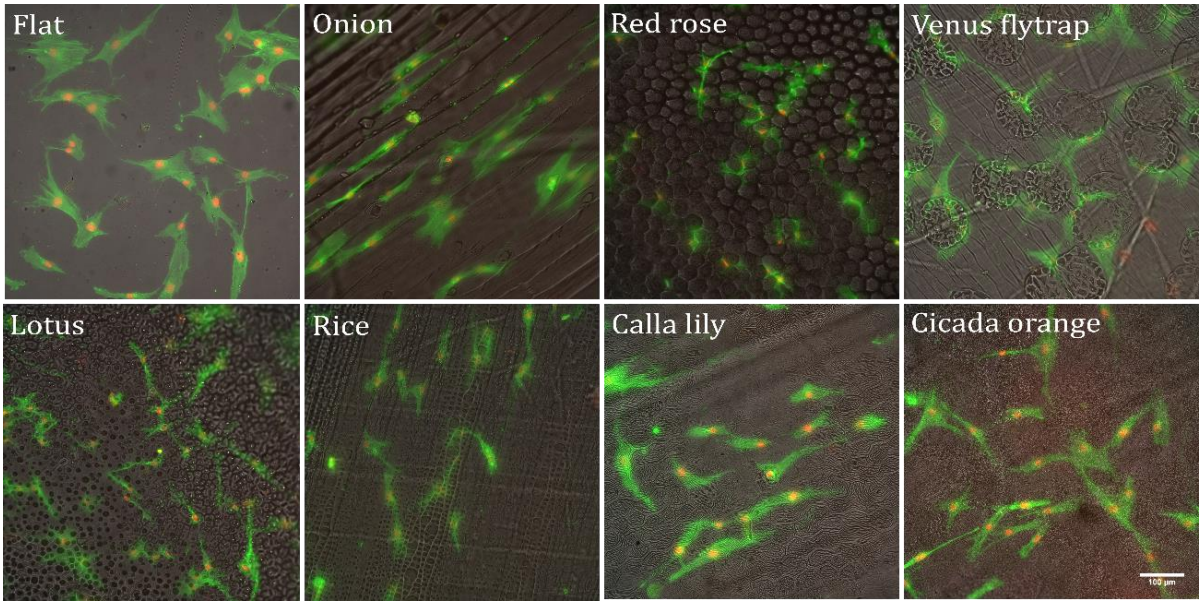

Figure 3. Visualisation of cells seeded on different natural topographies. BM-hMSCs were seeded on distinct surfaces for 24hrs. Composite brightfield-fluorescent images show the effect of the topographical features of the onion (*Allium),* red rose (*Rosa*), venus flytrap (*Dionaea muscipula*), holy lotus (*Nelumbo Nucifera*), rice (*Oryza sativa),* calla lily (*Zanthedeschia*) and cicada orange (*Gaeana festiva*) on cell size and morphology. Double staining for F-actin (green) and nuclei (red). Scale bar: bottom right, 100µm.

To further investigate the effect of natural topographies on cell shape, fluorescent image analysis was done to quantify the diversity in nuclear and cellular morphology among the distinct natural topographies and flat control. A robust CellProfiler pipeline was created that automatically analysed individual cells on each surface. From this pipeline, a total of 34 nuclear and cellular morphological

parameters were extracted. Cluster analysis of these parameters divided the natural surfaces into three groups, including two small clusters and one large cluster (Fig. 4A). One of the two smaller clusters consisted of the dung beetle (*Catharsius molossus*), orange beetle (*Euchroea auripigmenta*), giant cicada (*Quesada gigas*) replicas, while the other group included the red rose, hortensia (*Hydrangea*) and holy lotus surfaces. The large cluster was built up of several smaller subclusters and included the flat control surface. The cluster plot of the principal component analysis confirmed the same trend, forming three main clusters (Fig. 4B).

The heatmap of the clustering enabled to identify the morphological parameters responsible for the cluster pattern of the different surfaces (Fig. 5). Representative examples of these diverse cell and nuclear morphologies of the different clusters are given in Fig. 6. Natural topographies induced a wide variety of morphological changes compared to spread morphology with large nucleus and cell size observed on the flat control (Supp. Fig. 4; Supp. Fig. 5). The group including the red rose, hortensia and holy lotus surfaces showed the smallest nuclear size, as evident from the low scores on nuclear size parameters including the perimeter, radius, area and length (Fig. 5). For example, the mean nuclear area was smallest on these three surfaces, with a 2.0, 1.8 and 1.7-fold decrease in nuclear area compared to the flat control for the red rose, hortensia and holy lotus surfaces respectively (Supp. Fig. 4). Related to this, the nuclear eccentricity, which showed the elliptic nature of a nucleus, was highest on these surfaces. Interestingly, the differently sized micropapillae in this group forced the nuclei into confined spaces, as shown for the holy lotus and hortensia (Fig. 6). In addition, the mean cell area on these surfaces was also smaller than observed on other surfaces (Supp. Fig. 5). The 1.8, 1.9, 2.1-fold decrease in mean cell area compared to the flat control observed on the dung beetle, orange beetle and giant cicada replicas respectively partly explained their grouping tendency (Supp. Fig. 5). Next to their small size, cells on these surfaces displayed high values for solidity and extent (Fig. 5), which was linked to compact cell morphology with only small protrusions, as illustrated for the giant cicada (Fig. 6). Even within the largest cluster a great diversity in morphology was detected. One interesting subcluster was formed by the onion, reedmace and rice replicas. On these surfaces cells showed elongated and directionally dependent morphology along the multiple ridges and grooves of these surfaces, as illustrated for the onion in Fig. 6. Another example of a subcluster, including the cicada red and cicada orange replicas, was characterised by a large nuclear size but a small cell size (Supp. Fig. 4; Supp. Fig. 5). Furthermore, other unique morphologies on the sedum, calla lily and venus flytrap replicas were represented by circular nuclei, compact cell morphology and small nuclear sizes respectively. In short, a great morphological diversity was identified among the distinct natural topographies. This lead to different clusters which had similar effect on cellular and nuclear morphology.

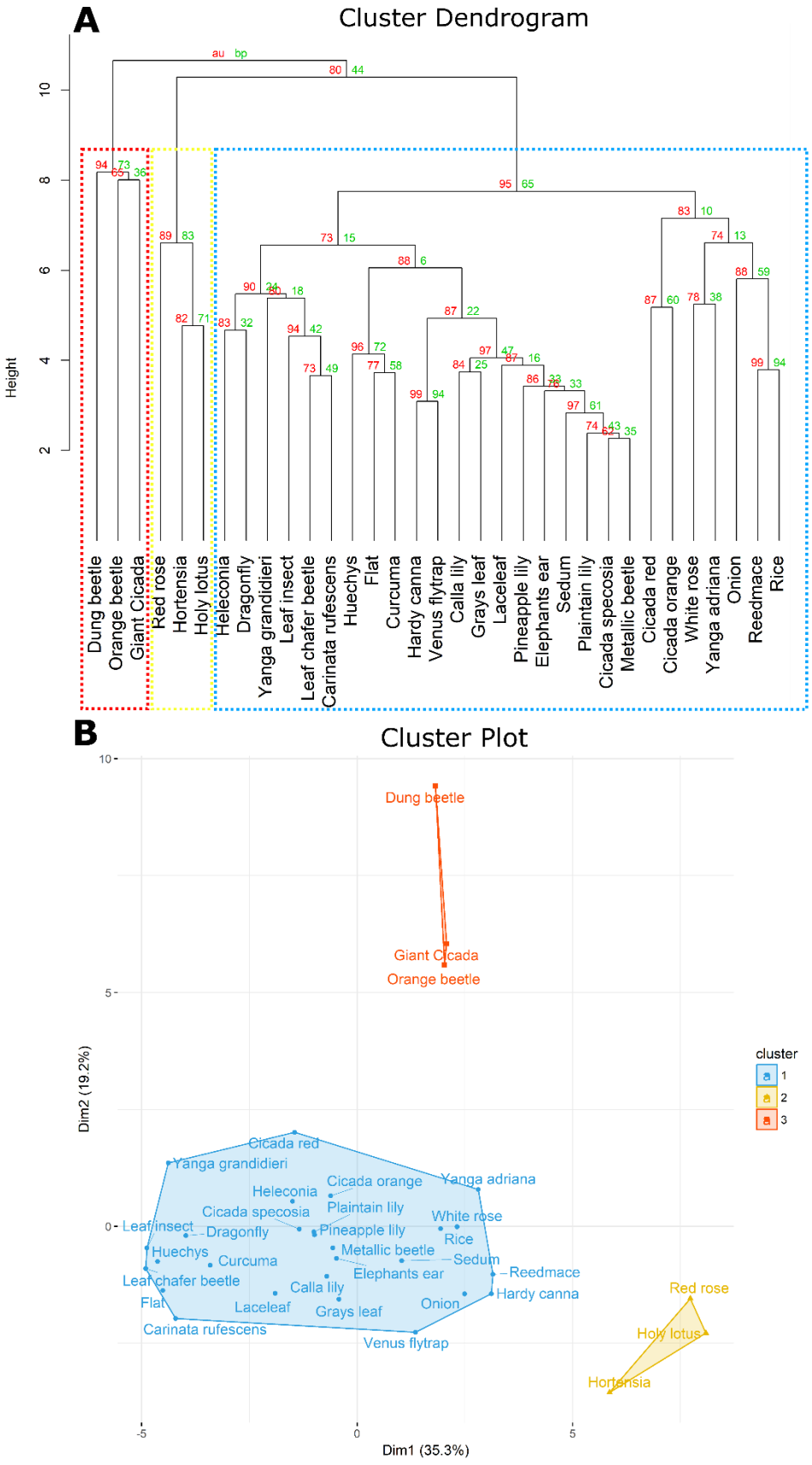

Figure 4. Cluster analysis of natural topographies based on cellular and nuclear morphology. (A) Cluster dendrogram of morphological data identified three main groups. Approximately unbiased (au) p-values in red and standard bootstrap (bp) p-values in green. **(B)** Principal component analysis revealed the same three clusters in a two-dimensional plot.

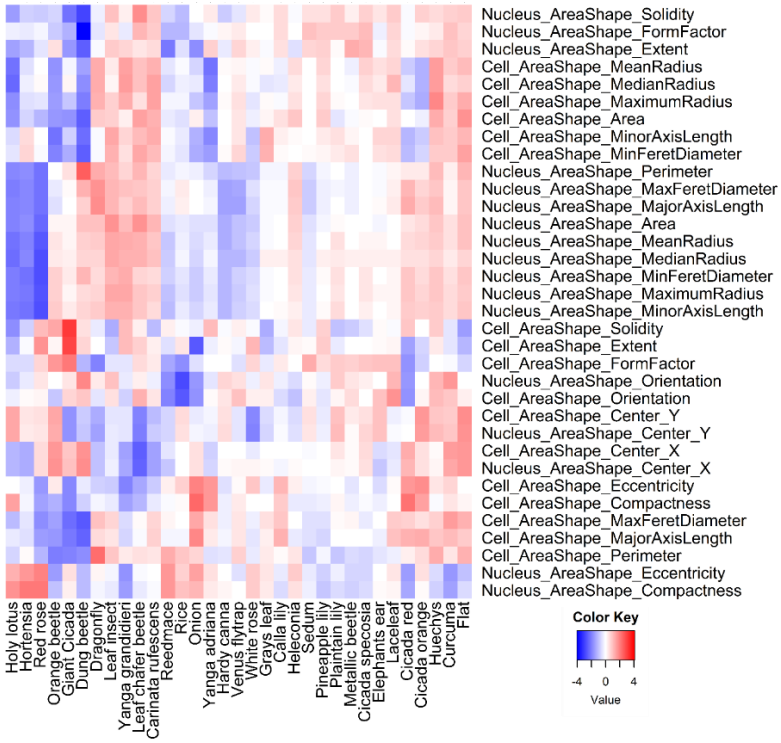

Figure 5. Heatmap of the morphological parameter profile of the distinct natural topographies. Identical distance metric and clustering method were used as for Figure 4.

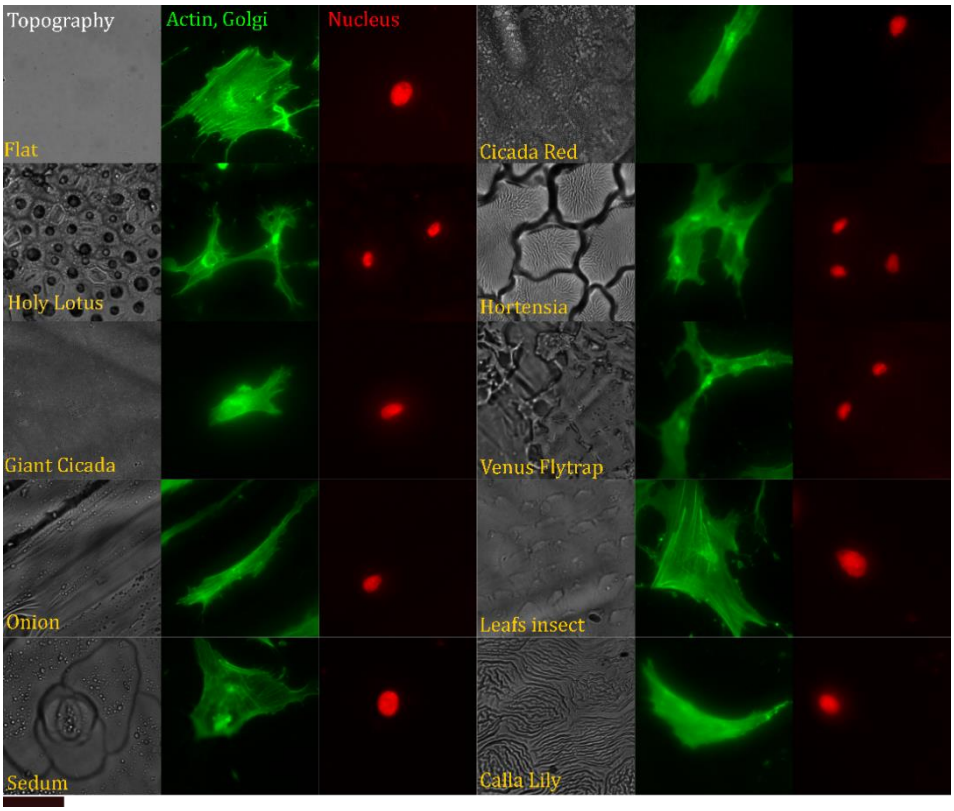

Figure 6. Representation of diversity in cellular and nuclear morphology among different natural surfaces. Brightfield images show natural topographies (left), while fluorescent images show actin (Phalloidin) and Golgi (WGA) (middle) or nuclear (Hoechst) (right) markers. Distinct topographies are indicated in yellow. Scalebar: bottom left, 50µm.

Natural surface topographies affect focal adhesion formation

The effect of surface topography on focal adhesion (FA) formation has been shown before and is often linked to cell shape[40–42]. To examine the effect of natural topographies on focal adhesion formation and organisation, BM-hMSCs were cultured on natural surfaces and flat control for 24hrs. Subsequently, cells were fixed and stained for actin (Phalloidin) and phosphorylated focal adhesion kinase (pFAK) targets. Quantitative fluorescent image analysis showed that focal adhesion formation per cell area varied between the different surfaces (Fig. 7A). In general, natural topographies induced an increased amount of focal adhesion formation compared to the flat control. Fluorescent visualisation showed that on the flat surface only a few focal adhesions were detected scattered around the cell (Fig. 8). In comparison, on the pineapple lily topography, an increased amount of focal adhesion of larger size were detected in the same cell size (Fig. 8). Topography affected focal adhesion formation despite the similar cell size. However, the organisation on this surface topography did not show a different pattern than the flat control. Analysis of the normalised distance from the FAs to the centroid of the cell allowed identification of surface topographies on which a distinct FA pattern formed (Fig. 7B). An increased distance to the centroid of the cell was observed for natural surfaces on which cells were elongated such as the rice and onion topographies. On the contrary, the distance of the focal adhesions to the centroid of the cell was smaller for surfaces that displayed compact cell shapes, including the previously described dung beetle and giant cicada replicas. Unique focal adhesion organisation was seen on the holy lotus replica. On this surface, focal adhesion formed around the micropapillae structures as indicated by the yellow arrows (Fig. 8). The focal adhesion organisation was linked to the cell shape on the holy lotus surface, grouping at the ends of the actin cytoskeleton. Overall, natural topographies guided focal adhesion formation and organisation.

The effect of natural surface topography on mouse embryonic stem cell pluripotency

Conventional methods to preserve differentiation of ESCs include the use of feeder-cells, gelatin (gel) and LIF[43,44]. Recently, the influence of topography on both pluripotent maintenance and differentiation of embryonic stem cells has been reported in literature[39,45–47]. The impact of natural topographies on mESCs pluripotency was investigated for the red rose, holy lotus, cicada *(Specosia)* and flat control. These topographies were selected because of their diversity both at the micro- and nanoscale. Pluripotent mESCs were exposed to three culture conditions: gel-coated surfaces with LIF, non-coated surfaces with LIF and non-coated surfaces without LIF in feeder-free condition. After three days of culture cells were fixed and stained for pluripotency marker Oct4. On the nanopillars of the cicada surface no cells adhered. Interestingly, on the three other surfaces including flat, Oct4

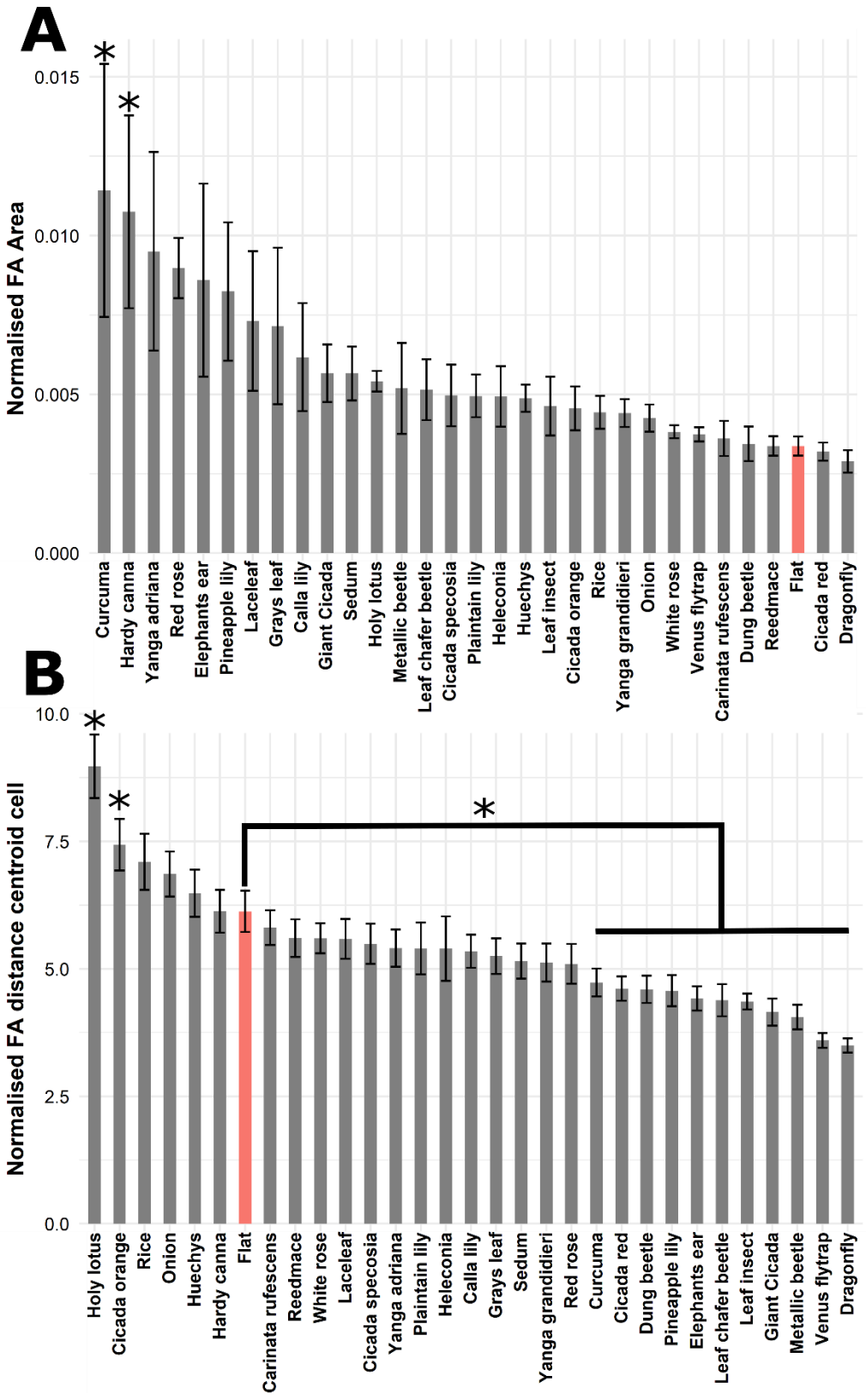

Figure 7. Effect of natural topographies on focal adhesion (FA) formation and organisation. (A) Quantitative analysis of normalised FA area between the different natural topographies (grey) and flat control (red) ranked from largest to smallest. Normalised FA area is defined as FA area divided by cell area. **(B)** Comparison of normalised distance to centroid among all surfaces and flat control. Normalised FA distance to centroid equals FA distance to centroid cell divided by mean cell radius. Error bars denote standard error of the mean. Pairwise t test: *p<0.05, Benjamini-Hochberg adjusted.

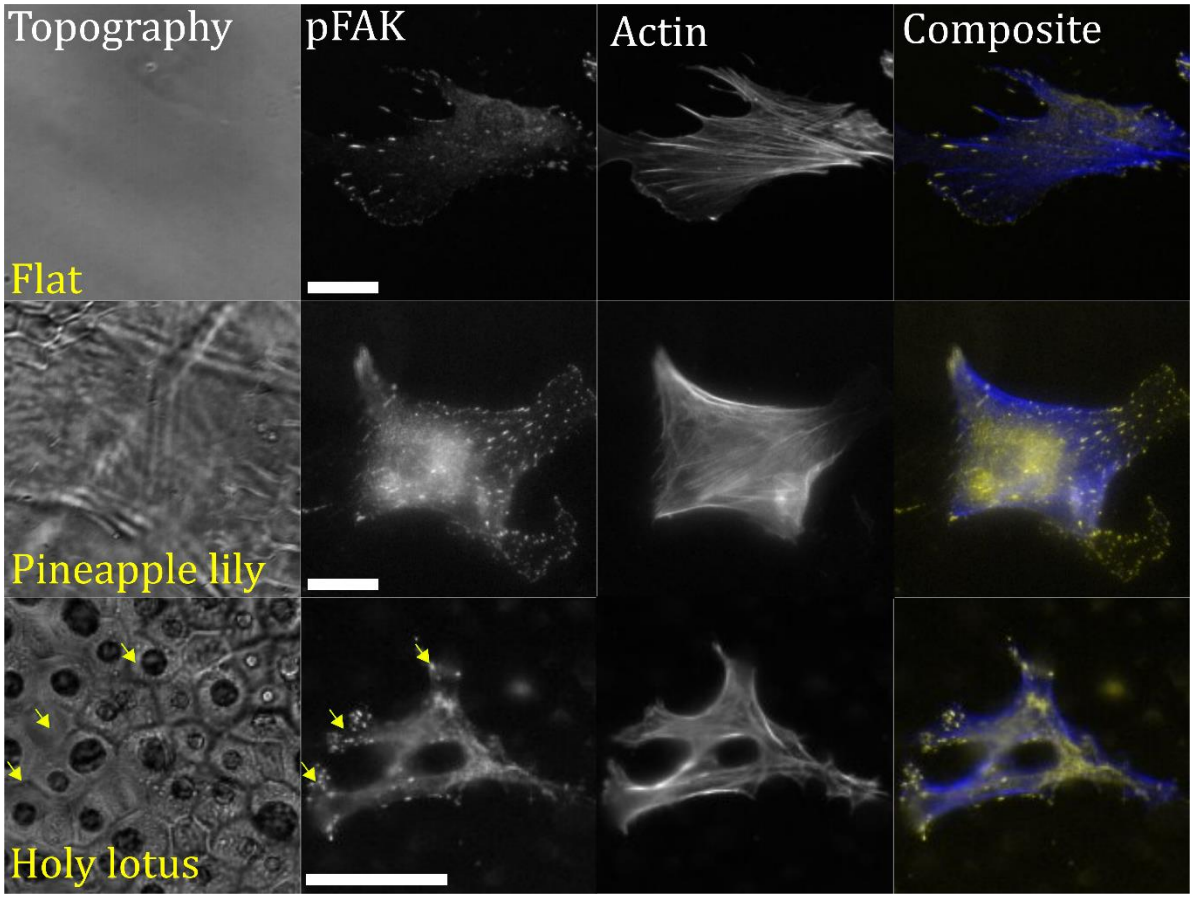

Figure 8. Visualisation of differences in focal adhesion formation and organisation between distinct surfaces. Representative examples of the holy lotus (*Nelumbo Nucifera),* pineapple lily (*Eucomis)* and flat control are shown. An increased FA formation is observed on the pineapple lily compared to flat. FAs are organised around the micropapillae of the holy lotus (indicated by arrows). Columns depict topography, pFAK, actin and composite images. Scale bars:50 µm.

expression increased for the +LIF -Gel condition (Fig. 9A). This was linked to the formation of small round colonies (Fig. 9B). Furthermore, a slight increase in Oct4 expression was observed in the other two conditions (Fig. 9A) compared to flat. The morphology of the colonies was affected by the natural topographies. Circular colonies formed around the distinct micropapillae of the red rose and holy lotus. This morphology was also observed for the -LIF -Gel condition, but for a smaller colony size. Colony size was largest for the flat surface in presence of LIF and gel. In short, Oct4 expression was slightly higher on natural topographies compared to flat. Colony morphology and size varied between the distinct conditions and surfaces.

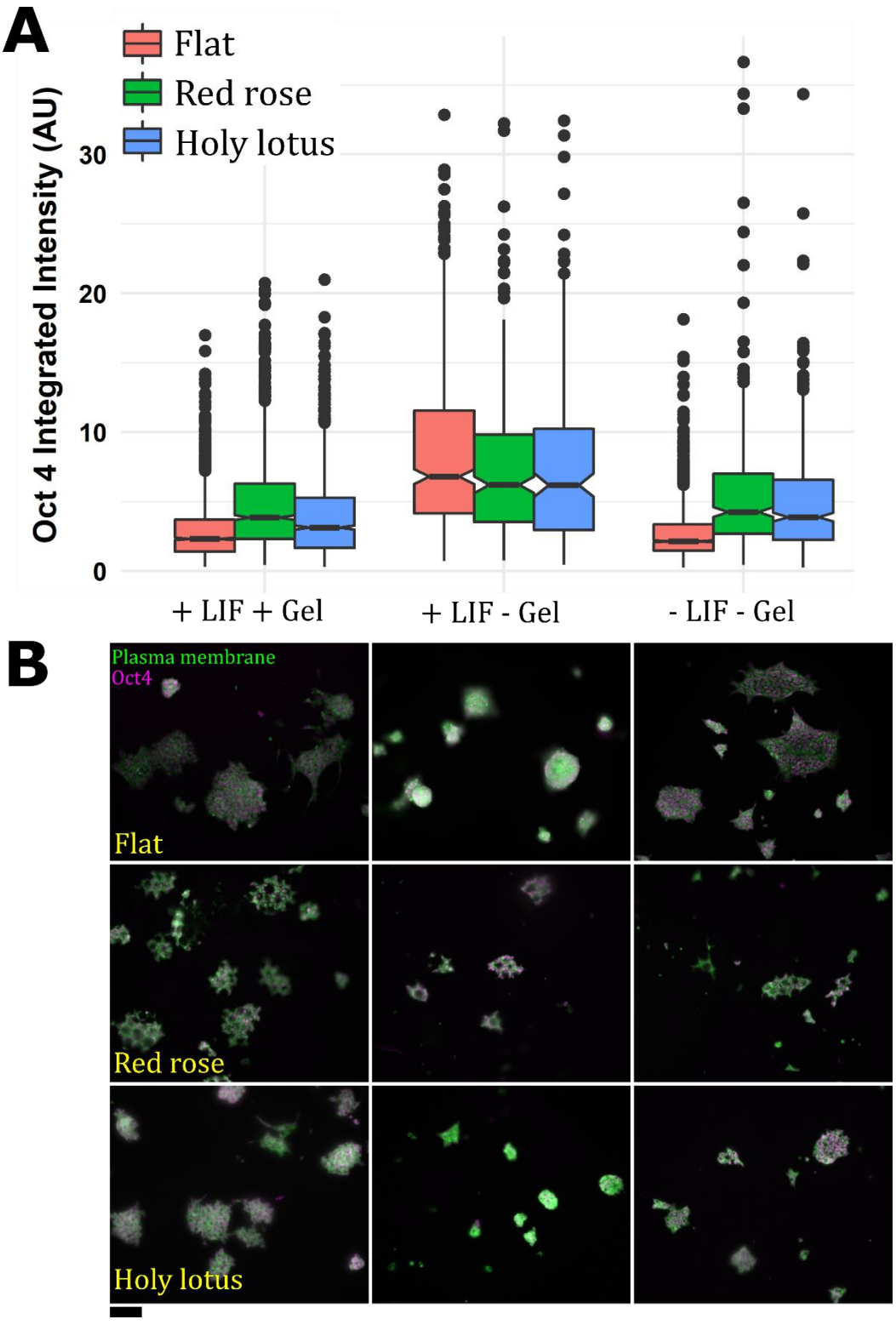

Figure 9. Effect of natural topographies on pluripotency and morphology of mESCs. Cells were seeded on flat, red rose and holy lotus surfaces in different culture conditions (+LIF +Gel, +LIF -Gel, -LIF -Gel). **(A)** Oct4 expression was quantified using integrated intensities of the Alexa Fluor 488 signal for each sample. Notched box plots are shown. **(B)** Visualisation of colony size and morphology for each condition per surface (Oct4 in magenta, Plasma membrane in green). Scale bar: bottom left, 50µm.

Natural topographies modulate *in vitro* cell differentiation

In literature, the impact of natural topographies on adipogenic and osteogenic differentiation of stem cells has been reported[48–50]. To investigate the effect of natural topographies on adipogenic differentiation of BM-hMSCs, cells were cultured on the distinct surfaces in adipogenic differentiation medium. After 21 days, fat formation was visualised using Oil red O staining. BM-hMSCs cultured on the flat surface in control medium showed no fat formation, whereas the counterpart cultured in presence of adipogenic differentiation medium displayed formation of fat droplets (Supp. Fig. 6). Interestingly, no to a negligible small amount of fat formation was detected for 27 out of the 32 natural surfaces examined. The percentage of cells that formed fat droplets was quantified for the other five natural surfaces and flat control (Fig. 10A). Among these five surfaces, a significantly higher percentage of fat positive cells was observed on the calla lily topography as compared to the H. incarnata, curcuma, laceleaf and C. rufescens topographies. Furthermore, the flat control showed a higher percentage of fat positive cells than the H. incarnata, curcuma, laceleaf and C. rufescens topographies, but a lower percentage of fat positive cells than the calla lily topography. Representative images of fat formation among these five surfaces are shown in Fig. 10B. An increased amount of fat droplets can be seen on the calla lily topography compared to the other natural surfaces. Altogether, five out of the 32 natural surfaces studied showed potential to induce adipogenesis in BM-hMSCs.

Next to adipogenic differentiation, osteogenic differentiation of BM-hMSCs was also examined on the different natural topographies. After osteogenic induction for 35 days, calcium deposition was visualised using Alizarin red staining. In absence of mineralisation medium cells cultured on the flat surface showed no mineralisation (Fig. 11, left). However, a small amount of mineralisation was observed on the flat surface in presence of mineralisation medium (Fig. 11, middle). Interestingly, very dense mineralisation was observed on the cicada specosia topography (Fig. 11, right). On all other natural surfaces no significant amount of calcium deposition was detected. In short, the natural surfaces did not promote osteogenic differentiation. Only the cicada specosia topography stimulated calcium deposition.

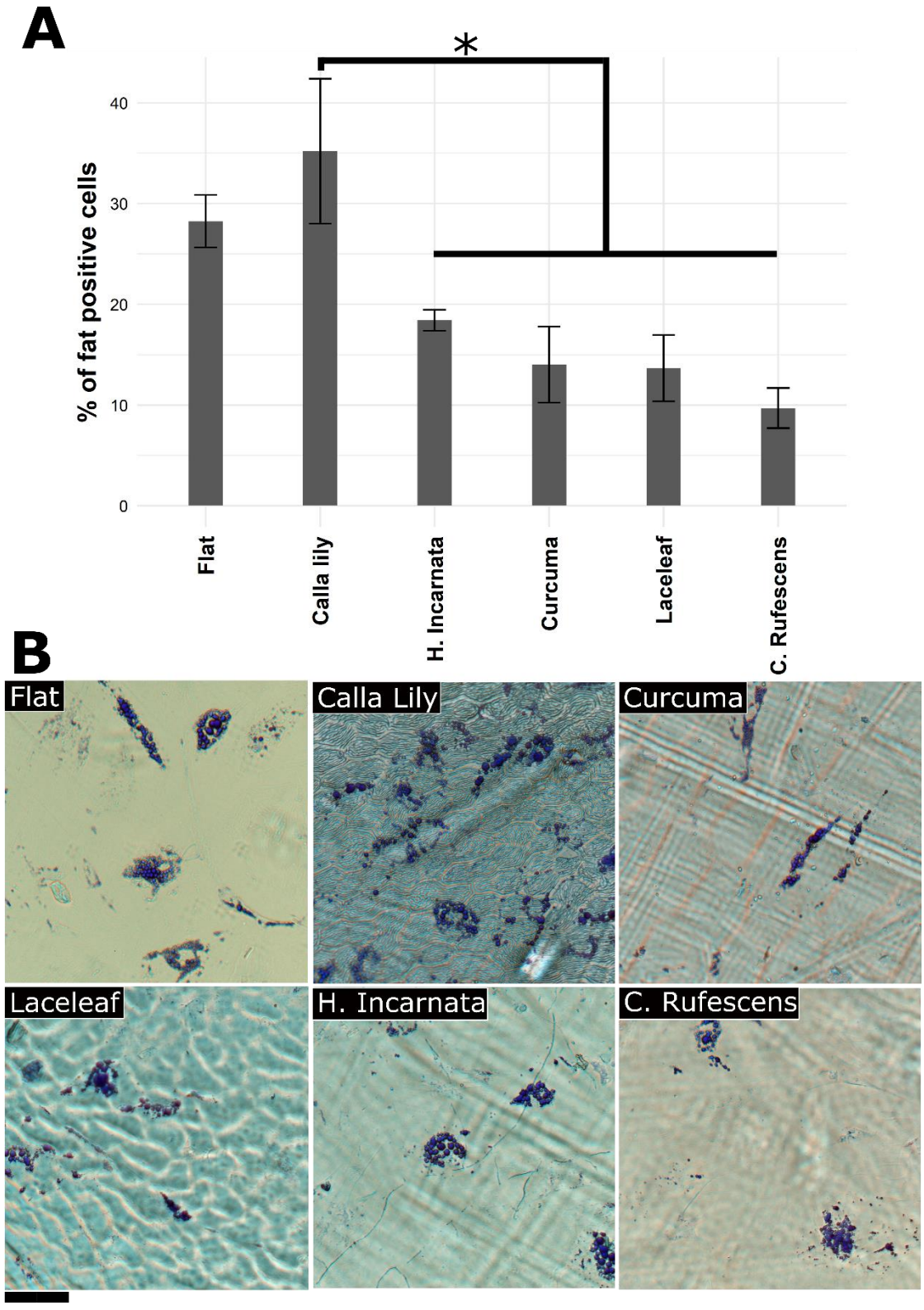

Figure 10. Influence of natural topographies on adipogenic differentiation of MSCs. MSCs were cultured on surfaces for 21 days in presence of adipogenic differentiation medium. **(A)** Fluorescent quantification of relative number of fat positive cells among natural surfaces and flat control. Adipogenic differentiation was significantly higher on the Calla Lily (*Zantedeschia*) as compared to all other natural topographies. Error bars denote standard error of the mean of three random areas quantified on each surface. Pairwise t test: *p<0.05, Benjamini-Hochberg adjusted. **(B)** Representative images of fat formation on natural topographies visualised using Oil red O staining. Scale bar: bottom left, 100µm.

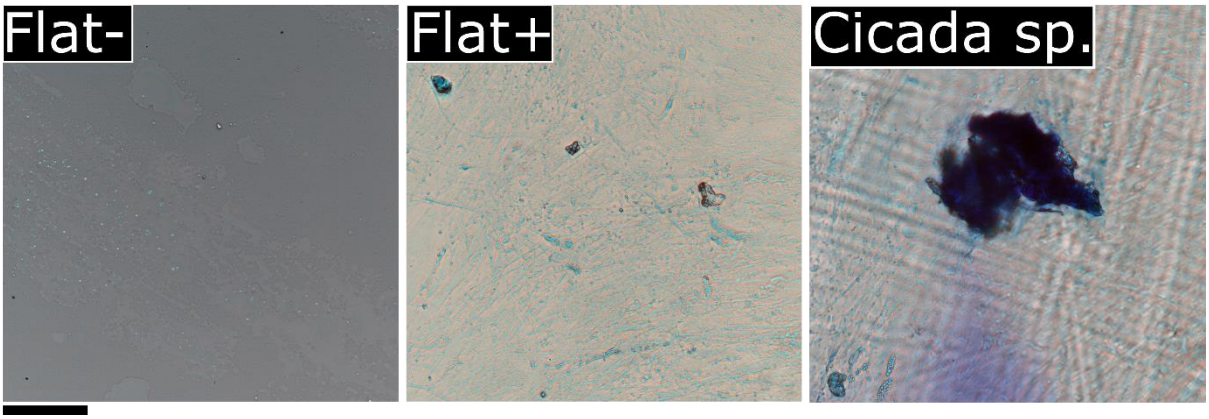

Figure 11. Images depicting mineralisation visualised using Alizarin red staining. Cells cultured on the flat surface in control medium showed no signs of calcium deposition (Flat-, left). A small amount of calcium deposition for the cells culture on the flat surface in mineralisation medium (Flat+, right). Dense mineralisation is observed on the Cicada (*Cicada specosia*). Scale bar: bottom left, 100µm.

Discussion

Material properties are often optimised to control cell behaviour in the field of regenerative medicine. A wide variety of inherent substrate parameters such as topography[10], chemistry[51] and stiffness[39] have shown to influence cellular processes. Identification of beneficial biomaterial characteristics remains a challenging task. Natural topographies gain interest because of their great variety in surface properties. The amount of disorder in these surfaces, including different degrees of surface roughness, show great potential to steer cell response. This study demonstrated that when cells are exposed to natural topographies a diverse range of cell responses are observed.

Replication of a large selection of natural topographies on a material suitable for cell studies was achieved by a hot embossing technique. This method allowed to expose cells to natural topographies and investigate their response. Topography is known to influence cell behaviour through cell shape[37–39]. Natural topographies induced a large diversity of cell shapes between different surfaces. Both nuclear and cell size were significantly affected by the distinct natural surfaces. Other studies have also reported changes in nuclear size due to environmental cues[52,53]. In addition, morphological parameters such as orientation and compactness varied among the natural surfaces. Heterogeneity proved to be an important factor to guide cell behaviour. Even within a relatively small selection of natural topographies, compared to artificial high-throughput systems, a great variety of cell responses were identified. Natural topographies forced cells into confined spaces or allowed them to adhere to small protrusions. Clustering of these surfaces via image analysis resulted in groups that generated similar cell shape. Heterogeneity of the natural surfaces also resulted in distinct cell shapes within a

surface. This could have an effect on the cluster analysis. However, topographical disorder can be a valuable property to stimulate stem cell differentiation[10].

Focal adhesion maturation and formation was altered by the natural topographies compared to a flat surface. The size per unit cell area increased for the majority of architectures. Furthermore, the organisation of the focal adhesions was highly influenced by topography. The cell formed around the distinct topographical features of the natural surfaces. On the flat surface the focal adhesion organisation was scattered around the cell. Similar observations were made by another study on the effect of surface microtopography on focal adhesion organisation[40]. This can have significant influence on cellular processes such as differentiation[42,54]. For instance, the anchorage mechanism of embryonic stem cell is highly important to maintain pluripotency[45]. When mESCs were exposed to natural topographies a slight increase in pluripotency marker Oct4 expression was observed for +LIF +Gel and -LIF -Gel culture conditions. However, increased culture periods should be implemented to confirm the ability of natural topographies to maintain mESCs pluripotency. In addition, the morphology of the mESCs colonies were round and smaller on the topographical surfaces. Colony morphology has been associated with both enhanced differentiation[55] and pluripotent maintenance of mESCs[56]. Furthermore, colony size is known to influence the differentiation trajectories of mESCs[57,58]. Interestingly, in absence of gel but in presence of LIF, increased Oct4 expression was observed for all surfaces. This could be associated with the adhesiveness of the substrate. In literature, it has been shown that strongly adhesive substrates (gel-coated) show lower expression levels of Oct4 compared to weakly adhesive substrates in presence of LIF[59]. Weakly adhesive substrates in absence of LIF and gel showed decreased pluripotency[59]. This trend was also observed for the flat control condition.

In vitro cell differentiation was modulated by the distinct natural topographies examined. In literature, it is known that nanotopographies promote pluripotent maintenance of MSCs[60,61]. On the contrary, both micro- and nanotopographies have shown to induce osteogenic and adipogenic cell differentiation[62,63]. Both adipogenic and osteogenic differentiation was prevented on most natural surfaces. However, it is possible that the cell donor had lost its multipotency. Repetition of a similar experiment with another cell donor is therefore advised. Furthermore, the screening of the 32 natural surfaces identified potential topographies that stimulated adipogenic or osteogenic differentiation. For example, the (micro)protrusions on the calla lily can be used in follow up experiments to stimulate adipogenesis in MSCs. In addition, the nanostructures on the cicada specosia are a potential candidate to promote osteogenic differentiation of MSCs.

In conclusion, a versatile method for replication of natural surfaces for cell studies was developed using hot embossing techniques. Cell behaviour greatly varied among the different copied natural

topographies. Firstly, natural architectures induced changes in nuclear and cellular size and shape. Furthermore, focal adhesion kinase formation and organisation was altered on natural surfaces. In addition, a slight increase in pluripotent maintenance of mESCs was observed on natural surfaces compared to flat. Finally, *in vitro* cell differentiation was modulated by the natural topographies. Further studies on the functional effects of natural topographies on cells are needed to confirm the possible applications of natural topographies. In addition, comparison of the effect of natural topographies to artificial topographies on cellular processes can give extra insights into their potential use for regenerative applications. Altogether, natural topographies allow for novel possibilities to examine cell behaviour not possible with conventional high-throughput methods.

Supplementary information

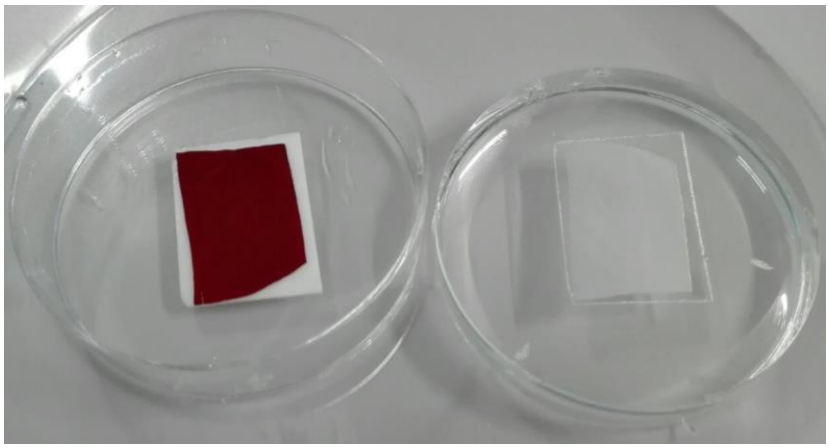

Supplementary Figure 1. Image of rose petal and corresponding PDMS mould containing negative imprint.

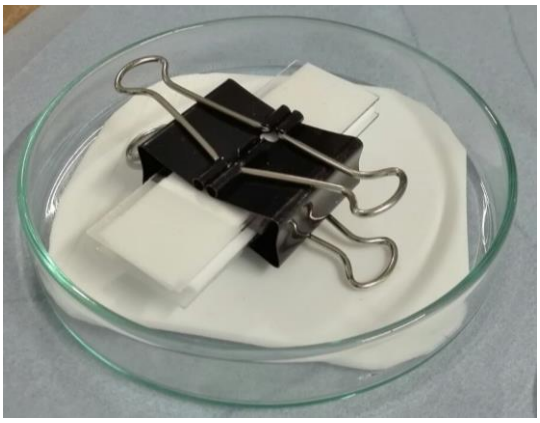

Supplementary Figure 2. Image of clamping system used to apply constant pressure.

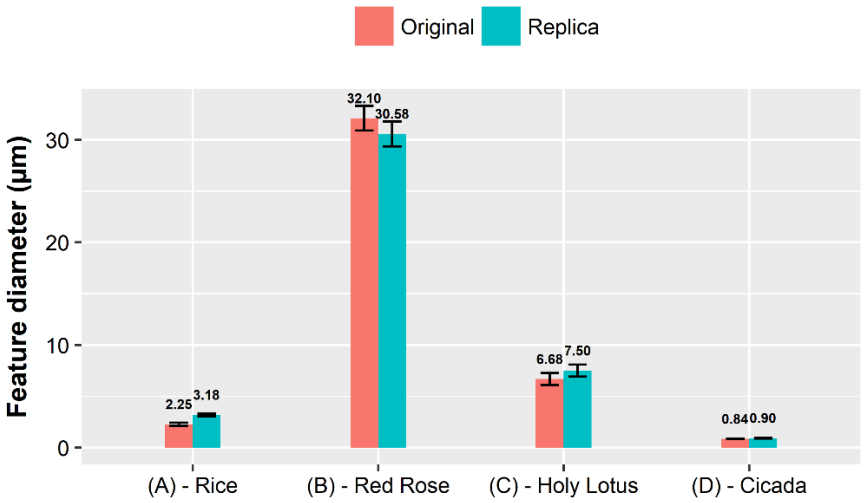

Supplementary Figure 3. Feature diameters of replicated and original natural surfaces. Diameters describing the micropapillea of the (*Oryza sativa)* (A), red rose (*Rosa*) (B), holy lotus (*Nelumbo nucifera)* (C) and the nanopillars of the cicada (*Yanga adriana)* (D). Error bars denote standard error of the mean (n=10).

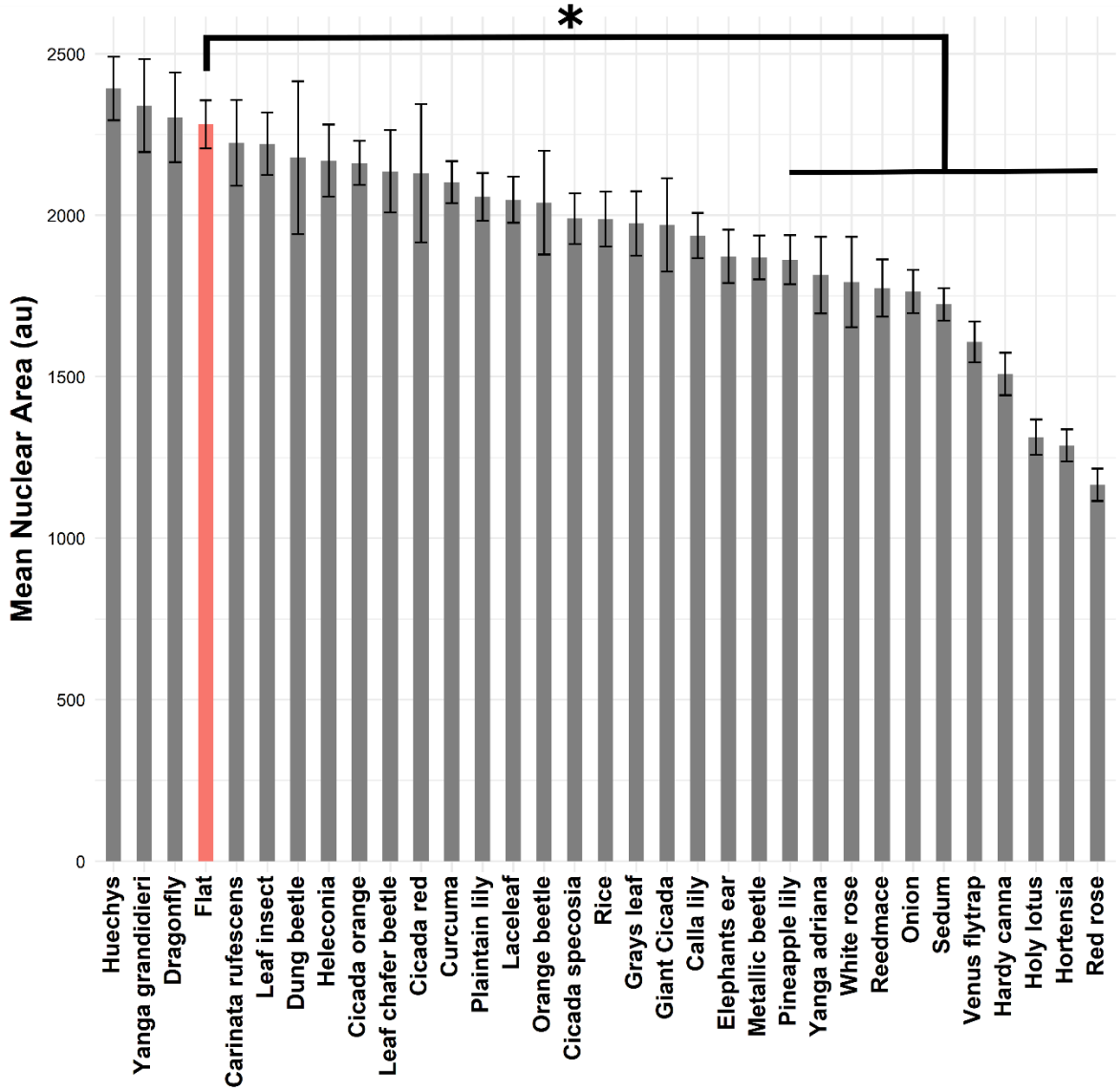

Supplementary Figure 4. Effect of distinct topographies on mean nuclear area. Analysis of mean nuclear area between the distinct natural topographies (grey) and flat control (red) ranked from largest to smallest. Tukey HSD test: *p<0.05. Error bars denote standard error of the mean.

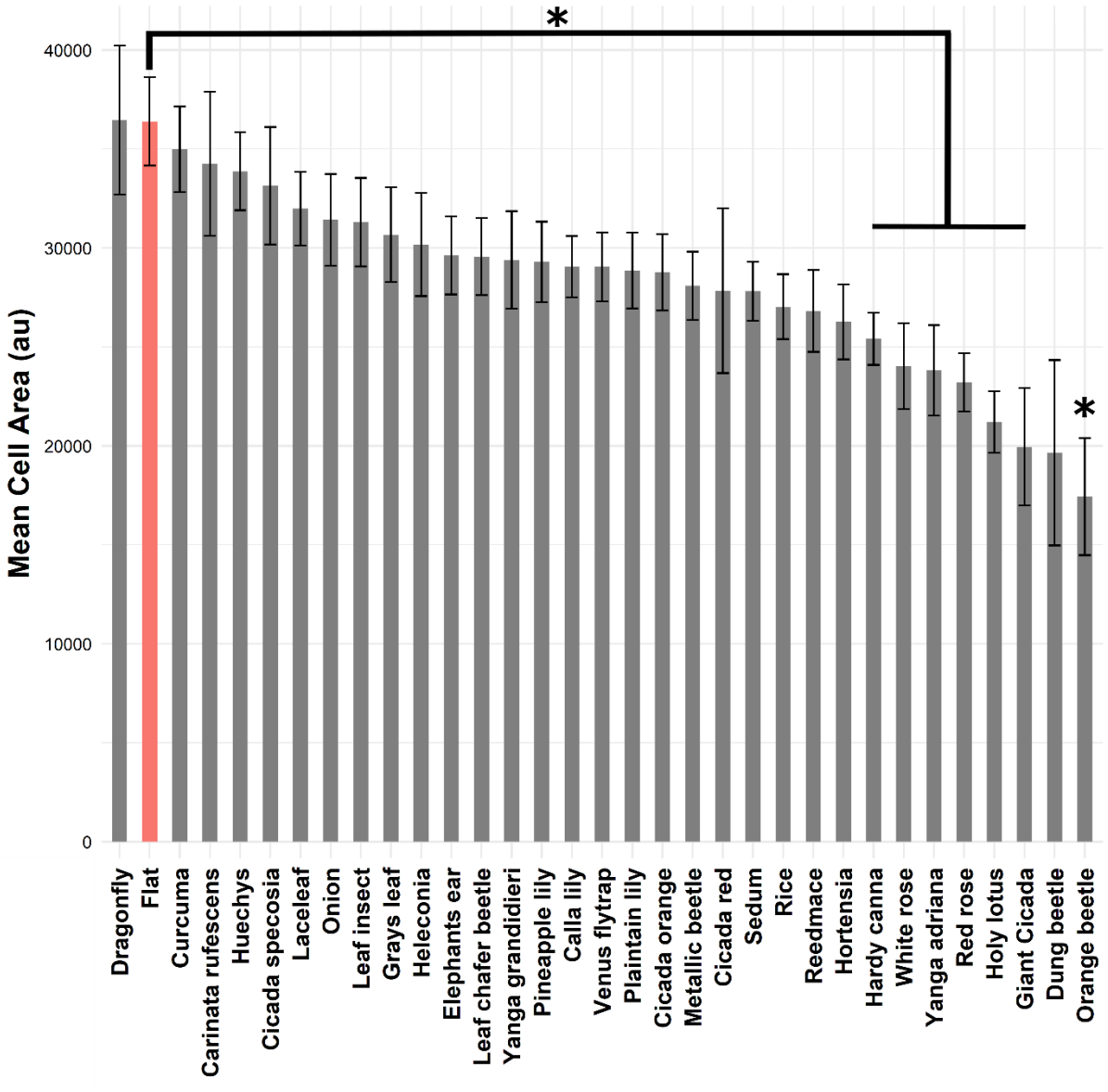

Supplementary Figure 5. Influence of natural topographies on mean cell area. Analysis of mean cell area between the different natural topographies (grey) and flat control (red) ranked from largest to smallest. Tukey HSD test: *p<0.05. Error bars denote standard error of the mean.

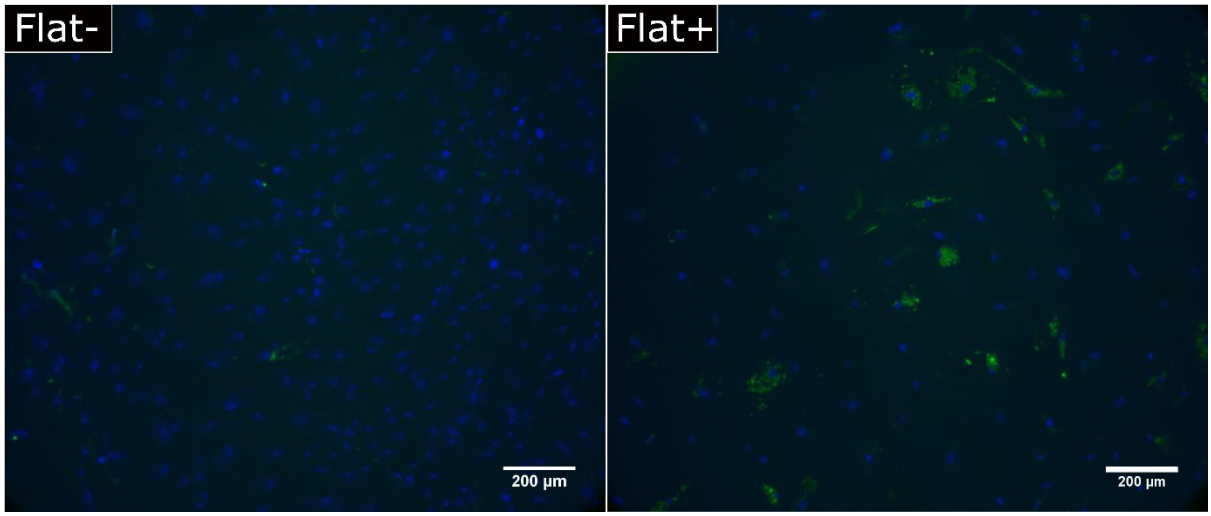

Supplementary Figure 6. Fluorescent visualisation of working of adipogenic differentiation medium. MSCs cultured in control medium showed no fat formation **(left, Flat-)**. MSCs cultured in adipogenic differentiation medium resulted in fat formation **(right, Flat+)**. Nuclei are stained with Hoechst (blue), fat droplets are stained using Oil red O (green). Scale bar: bottom right, 200µm.

Supplementary Table 1. SEM images depicting topographies of original natural surfaces and replicas.

Natural Surface	Original	Replica
 **Calla Lily** (Zantedeschia)	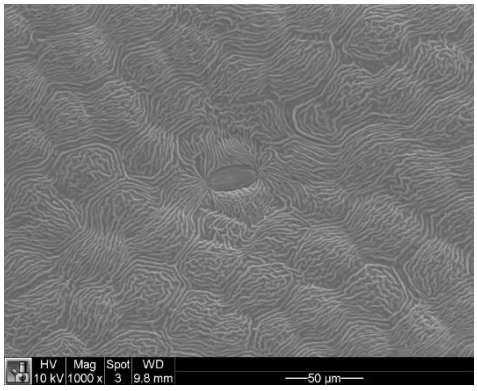	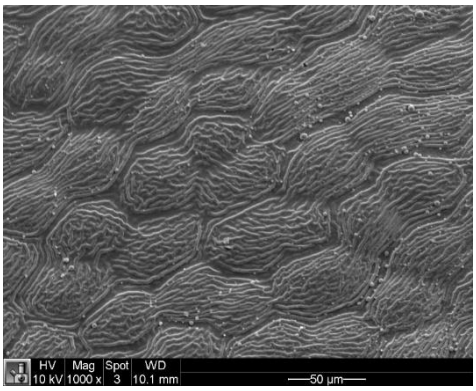
 **White rose**	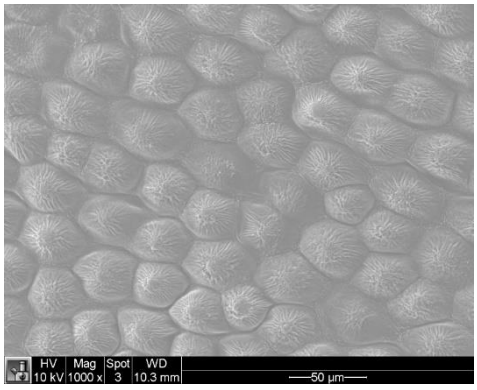	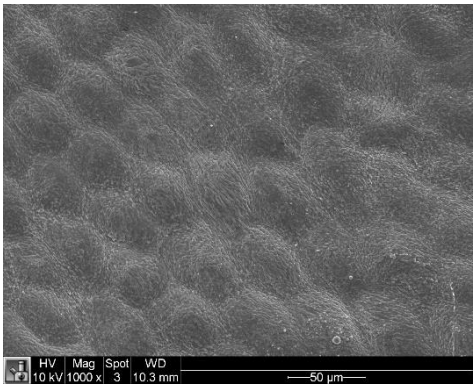

 **Hortensia** (Hydrangea)	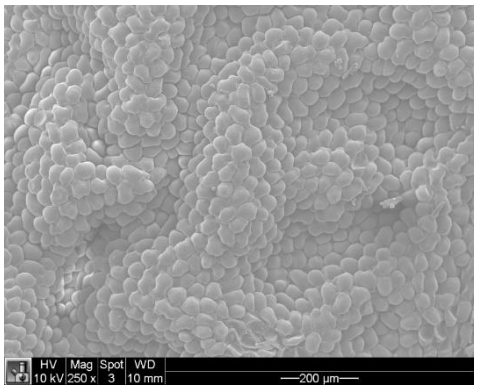	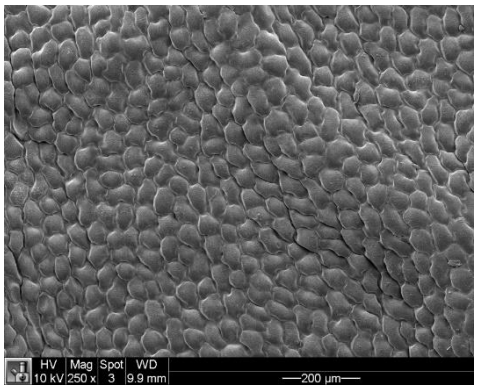
 **Red Rose** *(Rosea Rehd)*	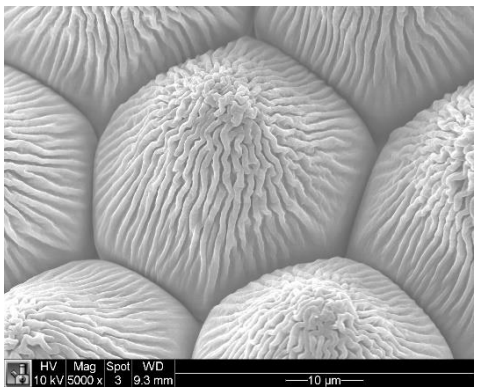	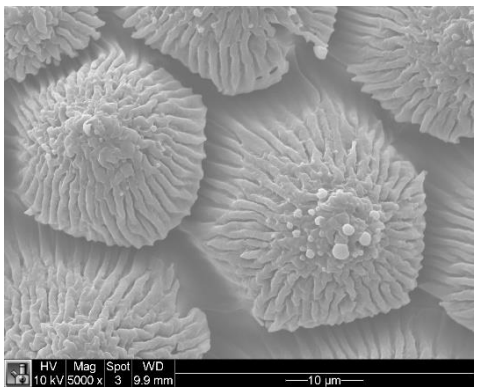
 **Laceleaf** (Anthurium)	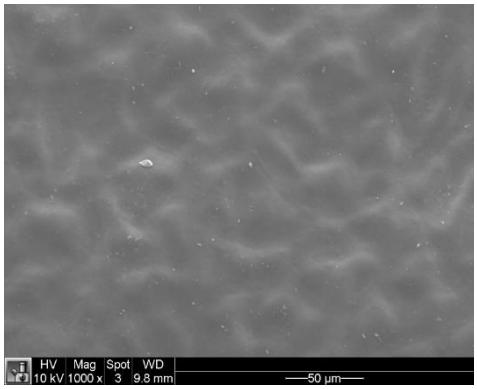	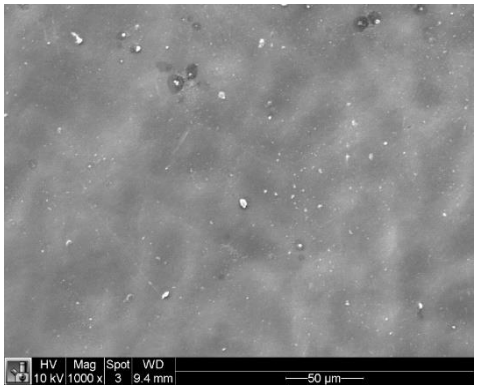
 **Curcuma** (Curcuma longa)	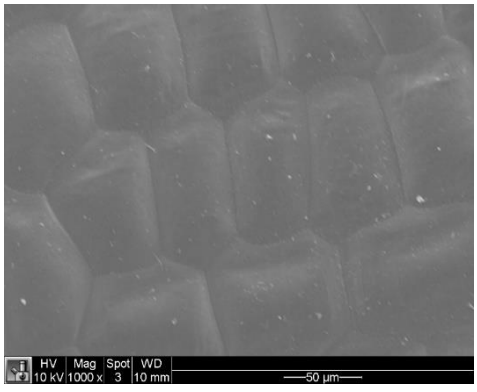	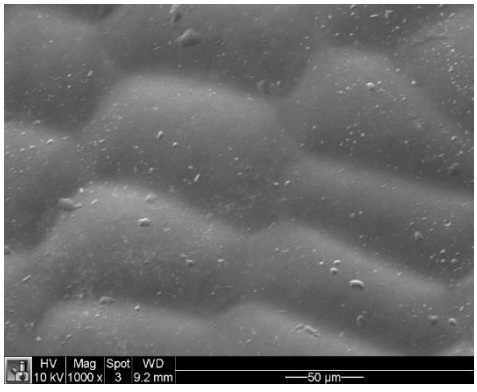

 **Heliconia** (Heliconia psittacorum)	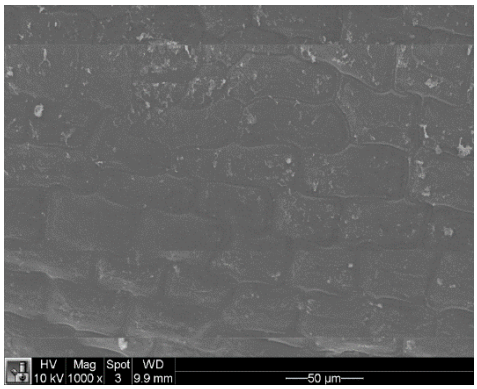	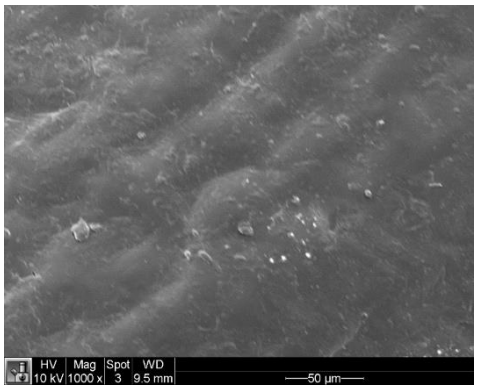
 **Pineapple Lily** (Eucomis)	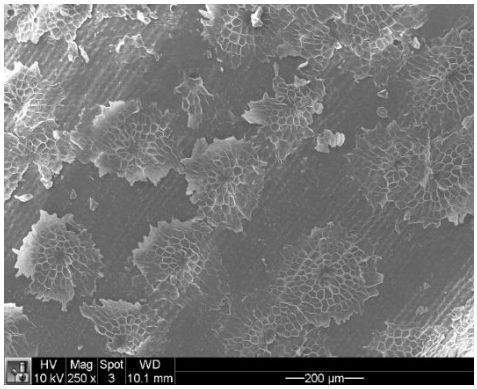	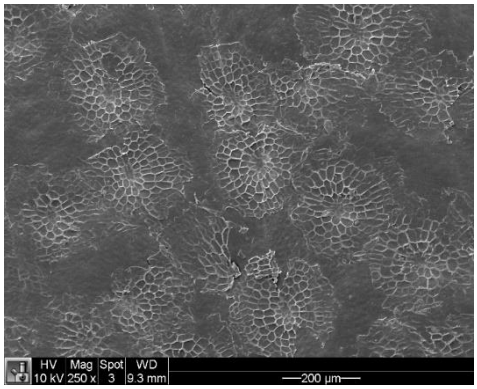
 **Elephant's ear** (Alocasia polly)	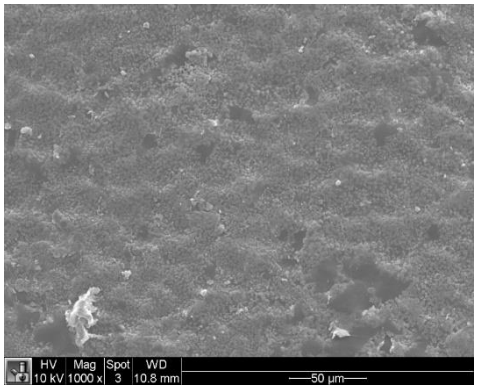	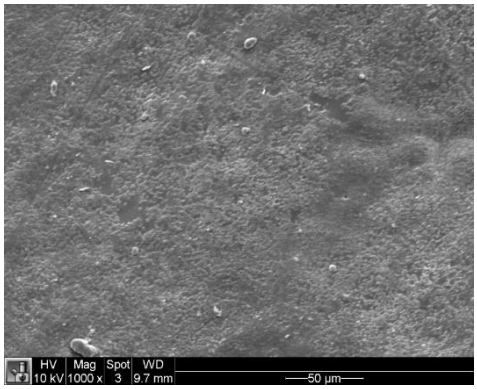
 **Reedmace** (Typha)	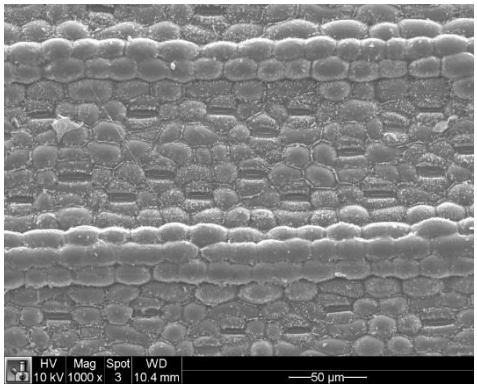	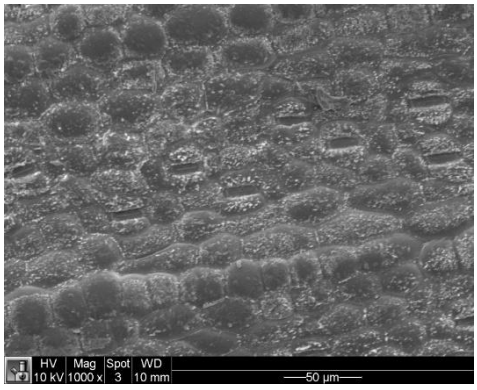

 **Sedum** (Euphorbia)	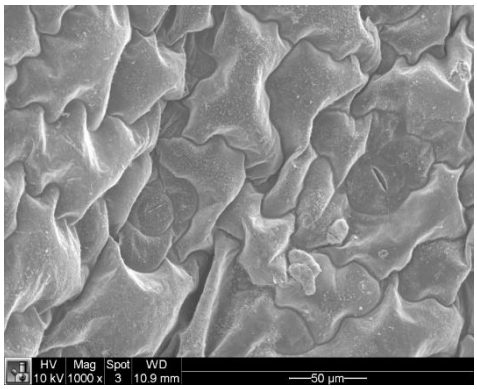	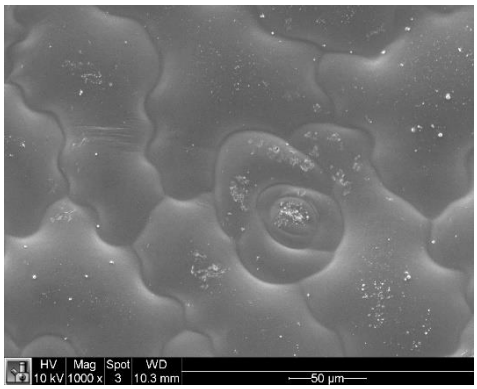
 **Onion** (Allium)	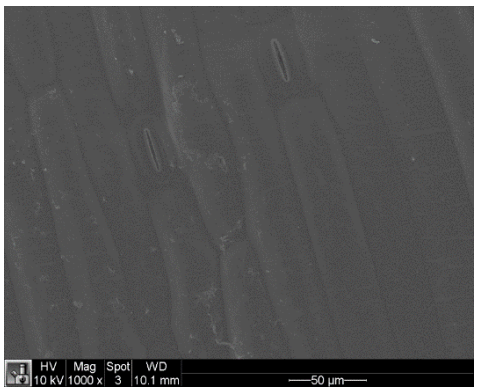	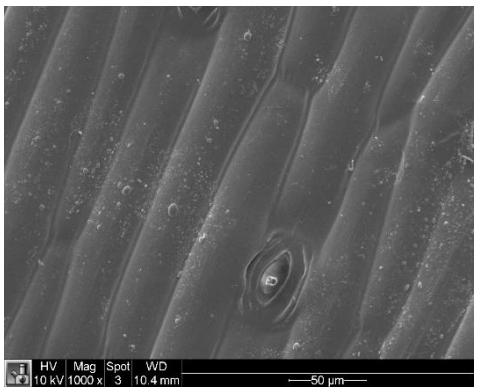
 **Holy Lotus** (Nelumbo nucifera)	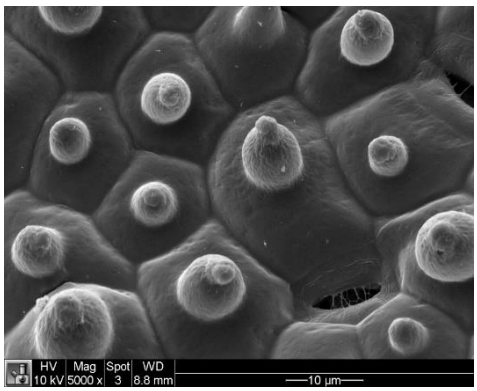	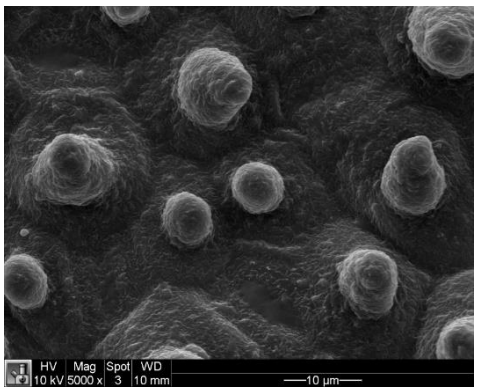
 **Rice** (Oryza sativa)	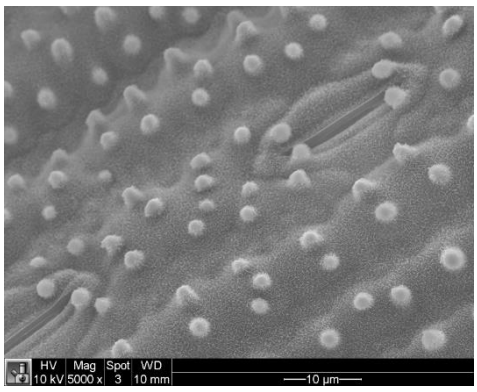	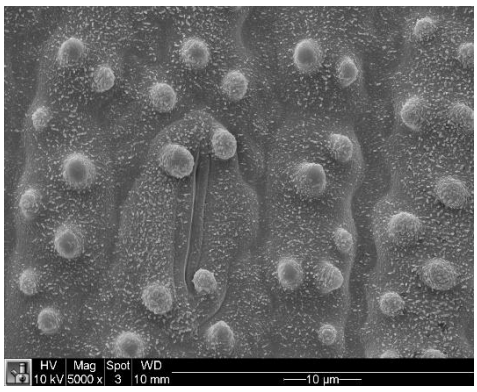

 **Plaintain Lily** (Hosta sp.)	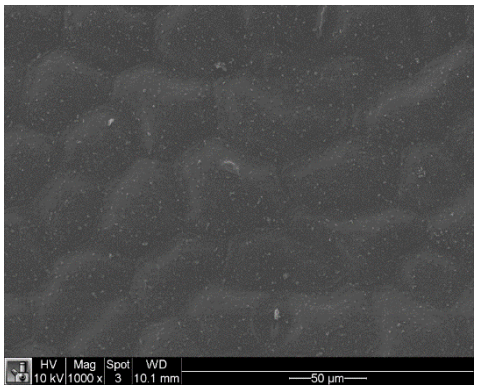	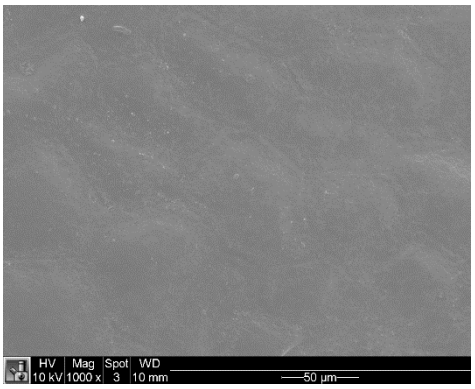
 **Hardy Canna** (Thalia dealbata)	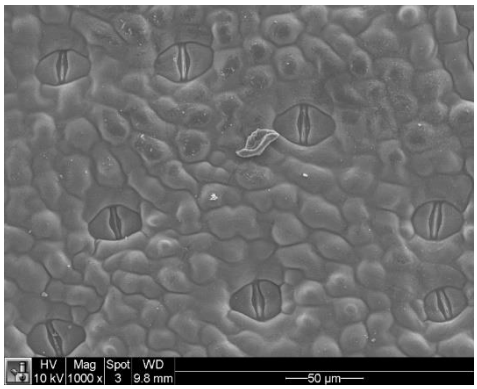	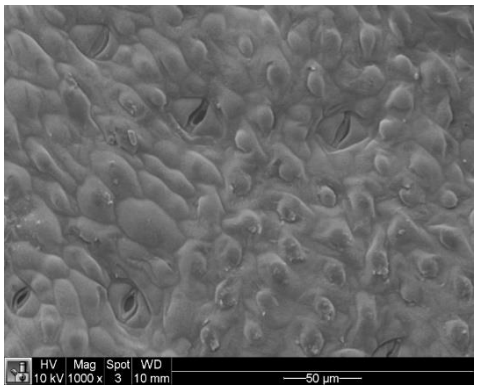
 **Venus flytrap** (Dionaea muscipula)	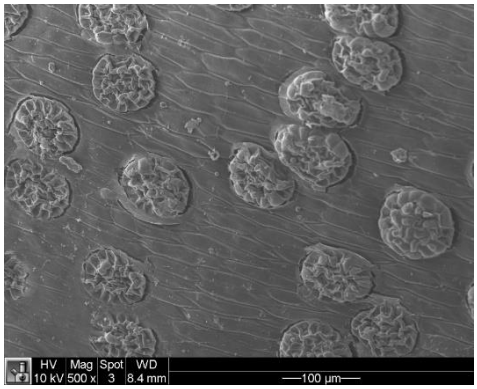	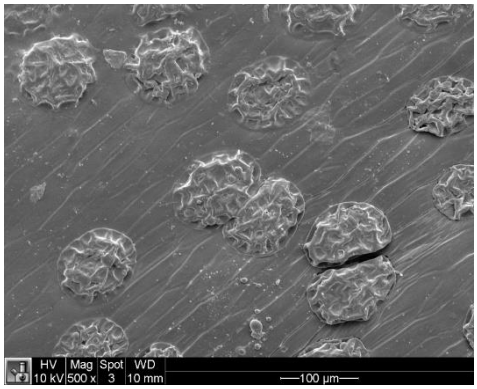
 **Cicada** (Cicada specosia)	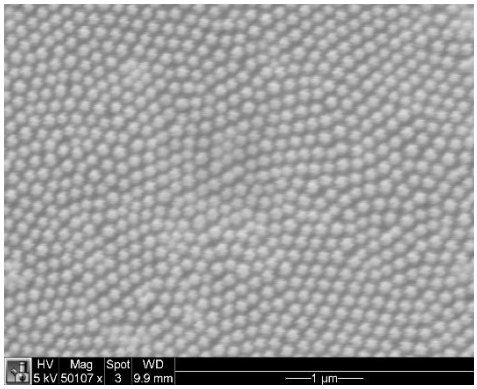	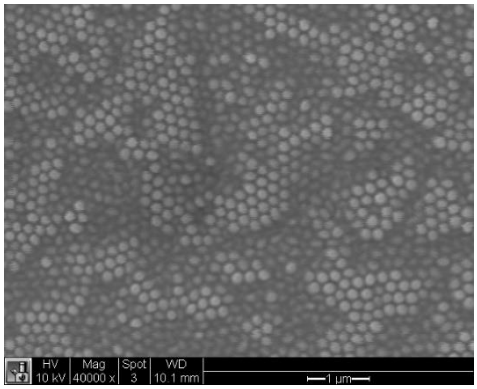

 **Metallic wood-boring beetle** (Megloxantha bicolor)	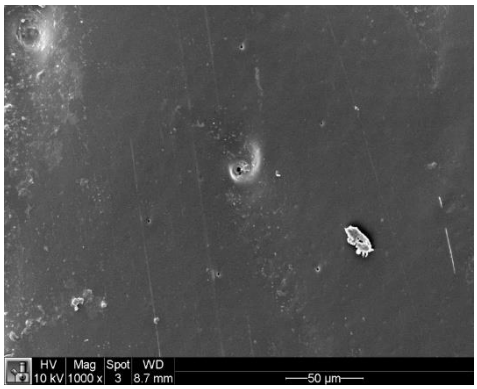	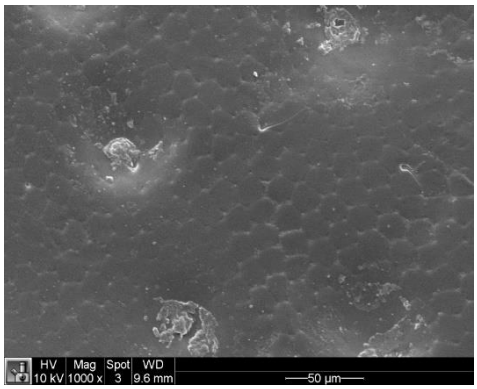
 **Shining leaf chafer beetle** (Chrysophora chrysochlora)	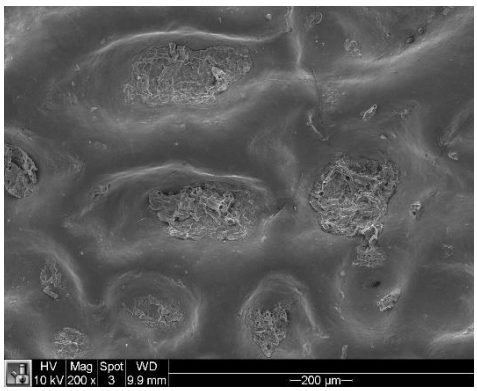	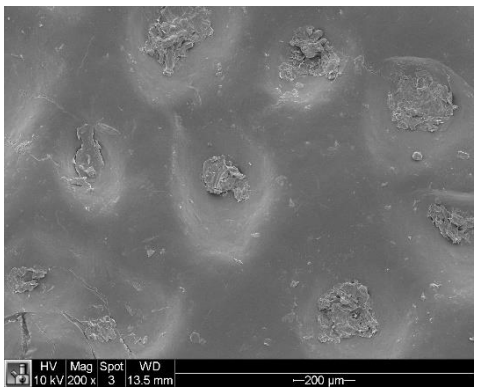
 **Dung beetle** (Catharsius molossus)		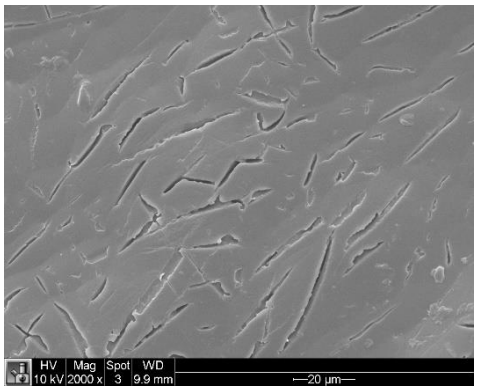
 **Orange flower beetle** (Euchroea auripigmenta)	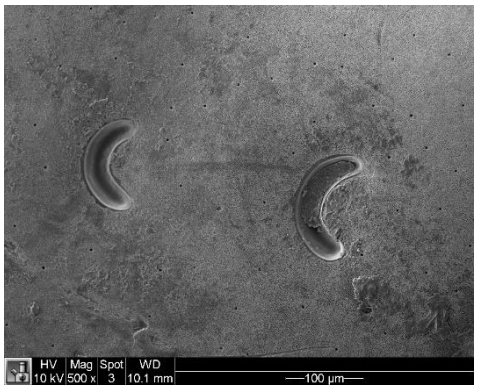	

 **Cicada red** (Gaeana festiva)	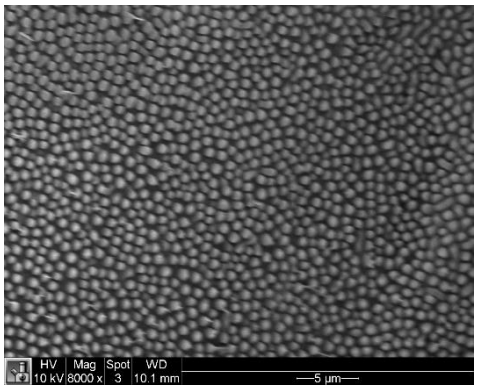	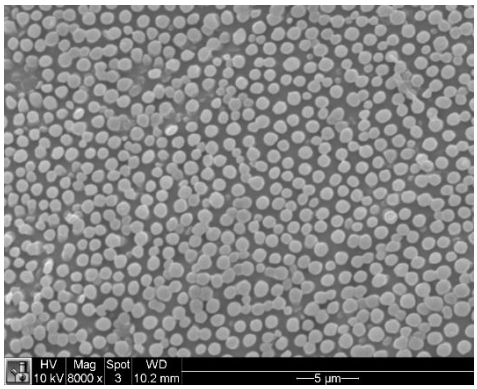
 **Cicada orange** (Becquartina electa)	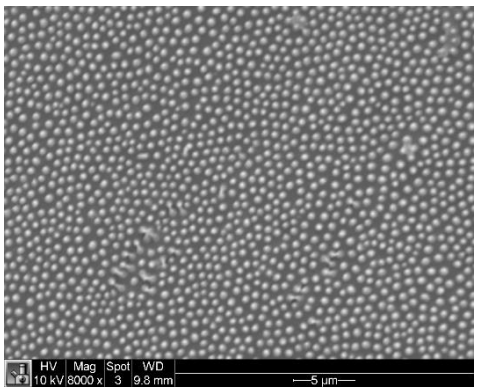	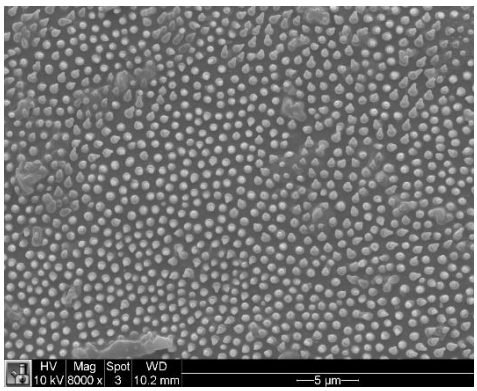
 **Giant cicada** (Quesada gigas)	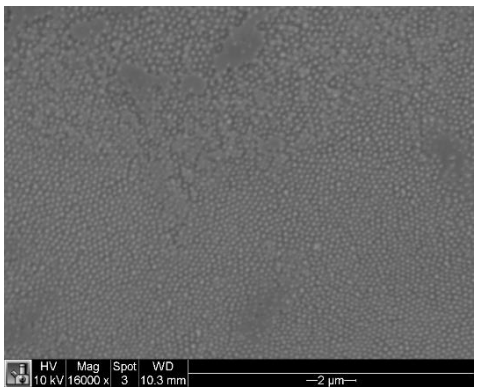	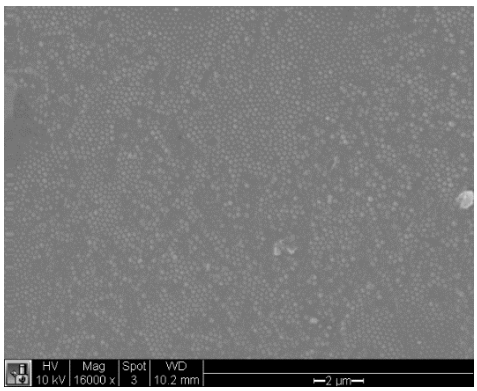
 Huechys incarnata	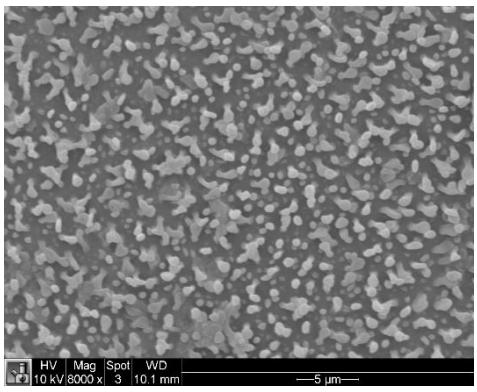	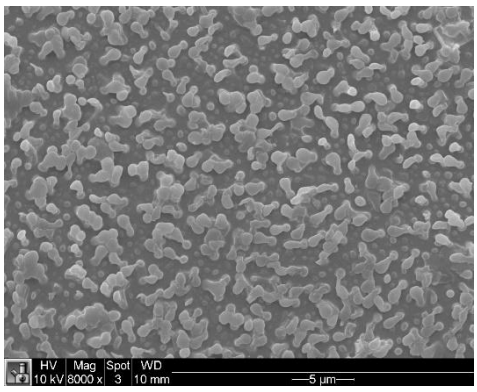

 (Yanga adriana)	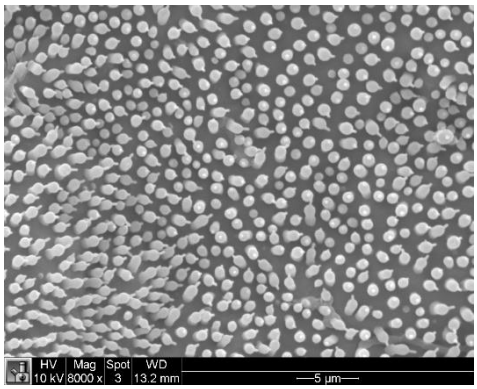	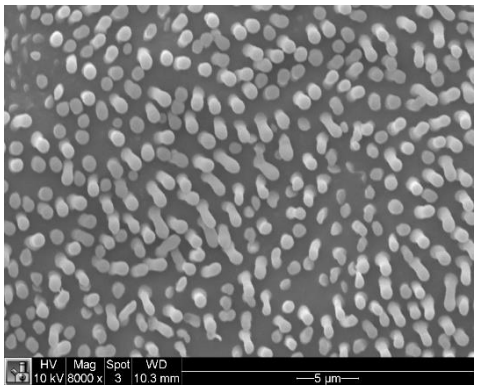
 (Yanga grandidieri)	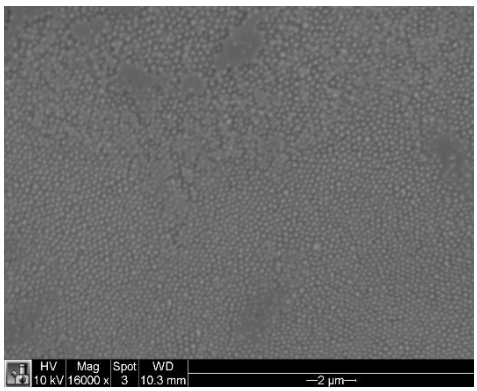	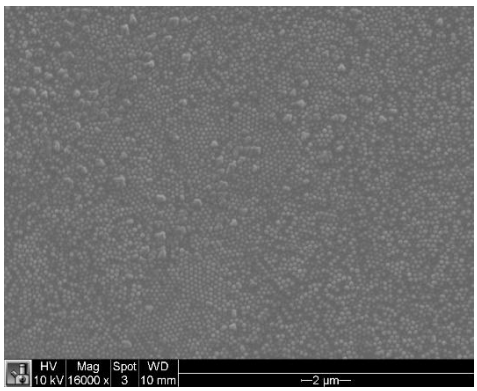
 (Carinata rufescens)	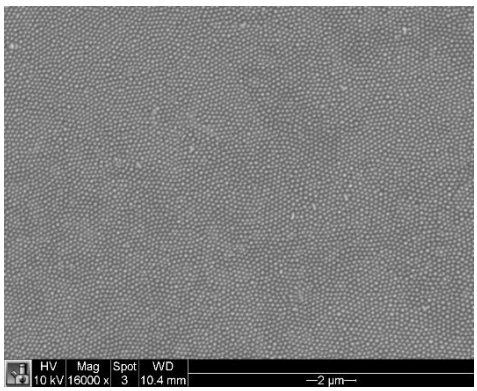	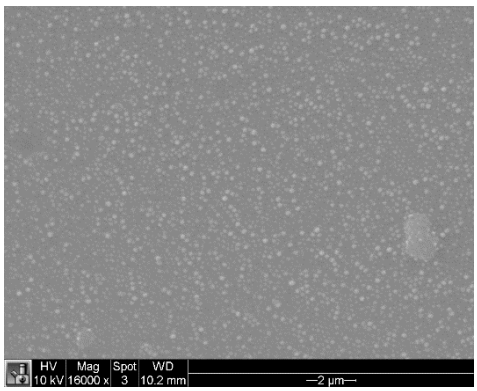
 **Dragonfly** (Odonata ssp)	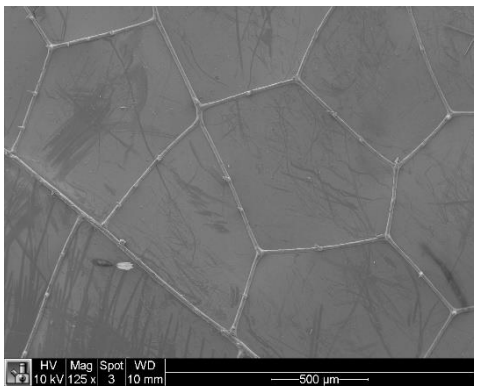	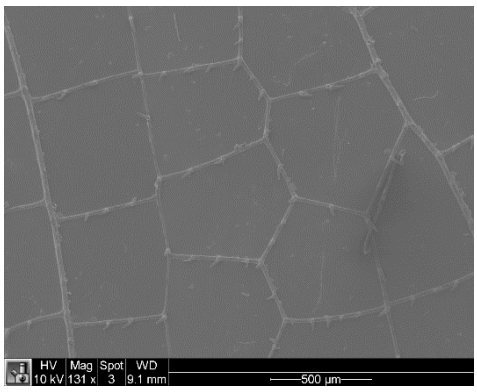

 **Gray's leaf** (Phyllium bioculatum)	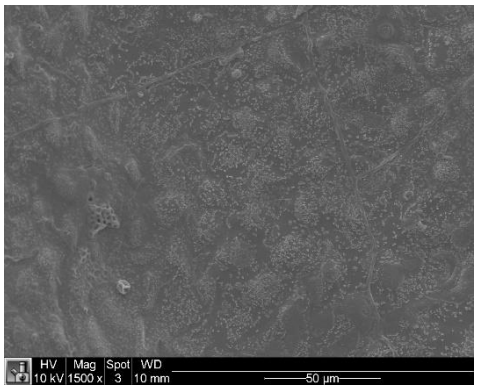	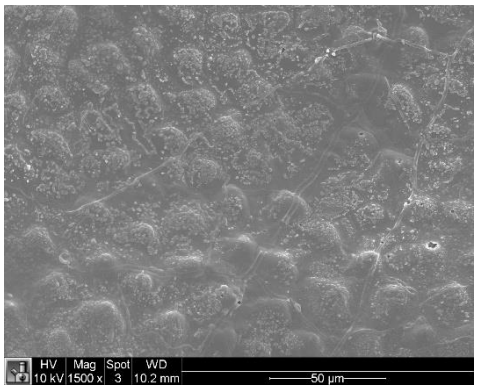
 **Leaf's insect** (Phyllium westwoodii)	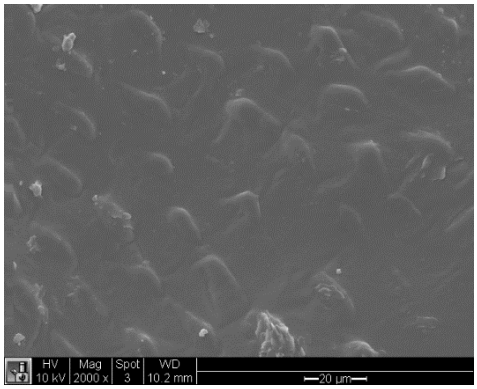	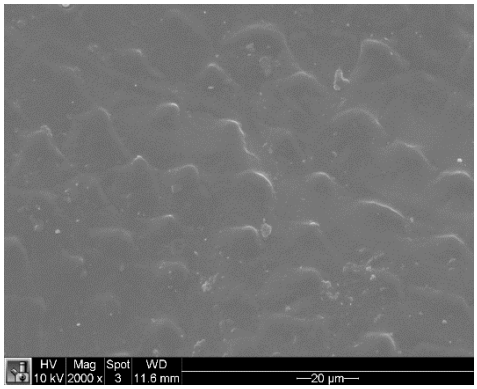

Supplementary Table 2. 3D profilometry images depicting topographies of original natural surfaces and replicas.

Natural Surface	Original	Replica
Calla Lily	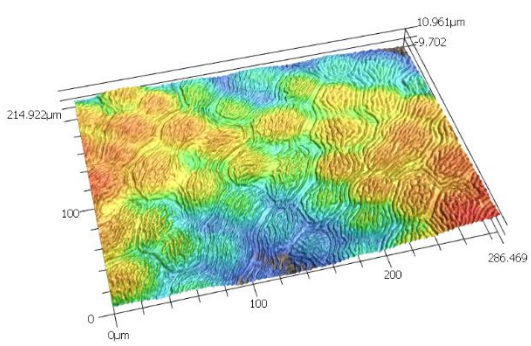	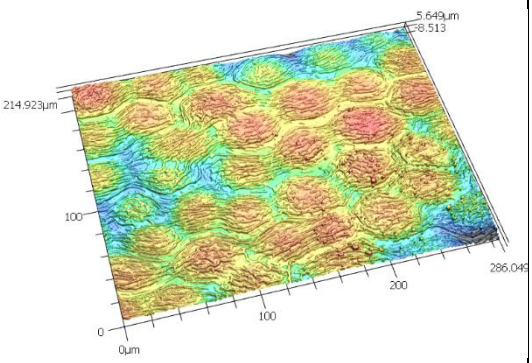
White rose	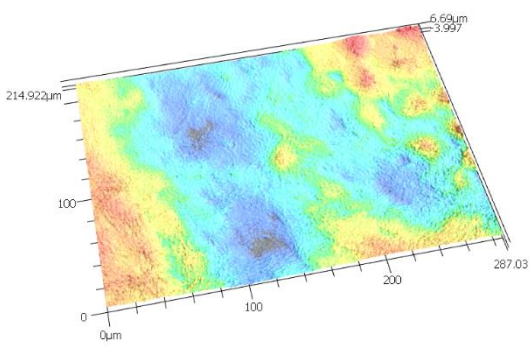	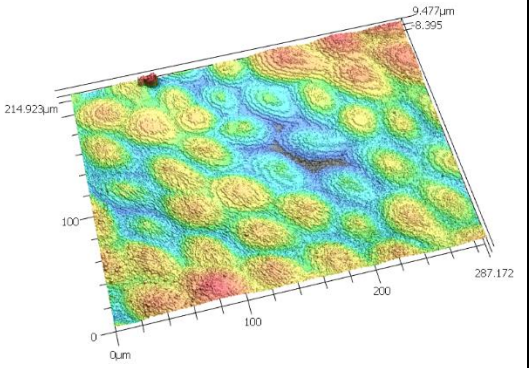
Red Rose	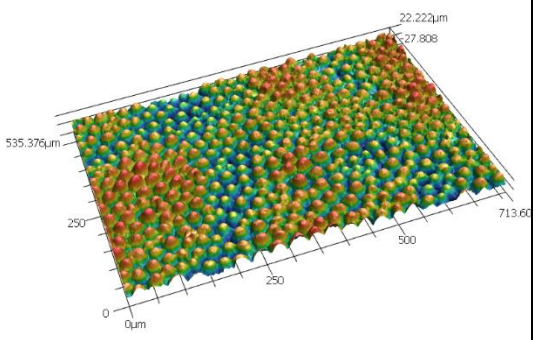	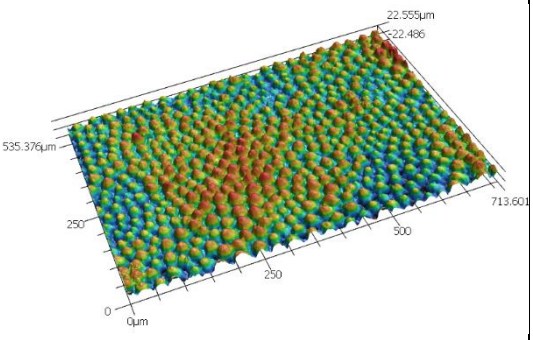
Laceleaf	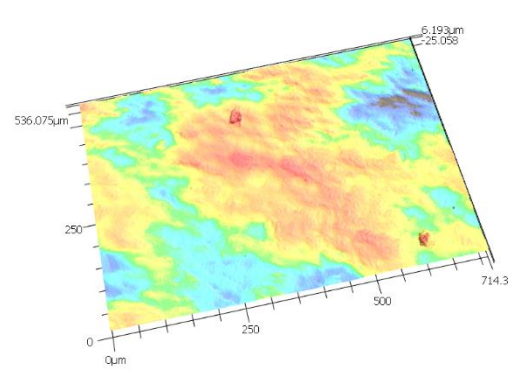	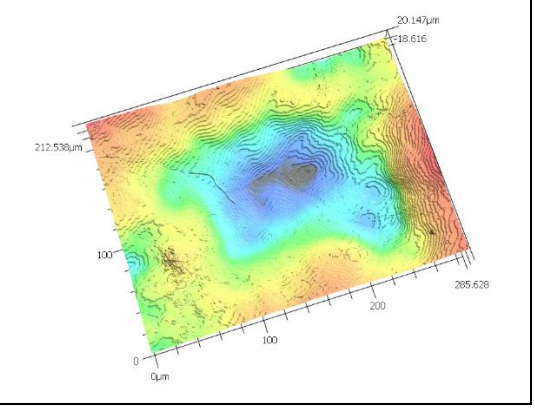

Curcuma	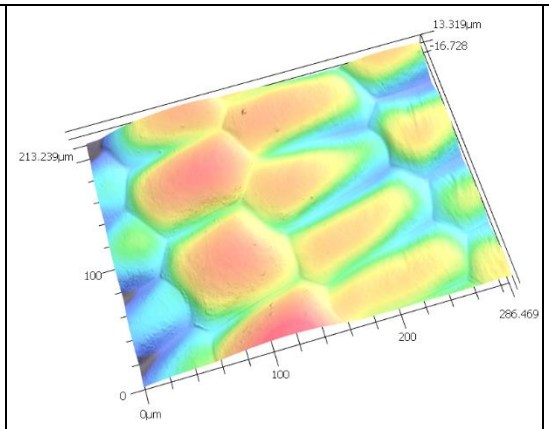	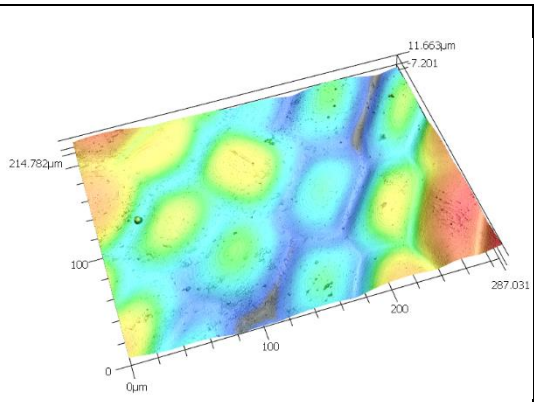
Heliconia	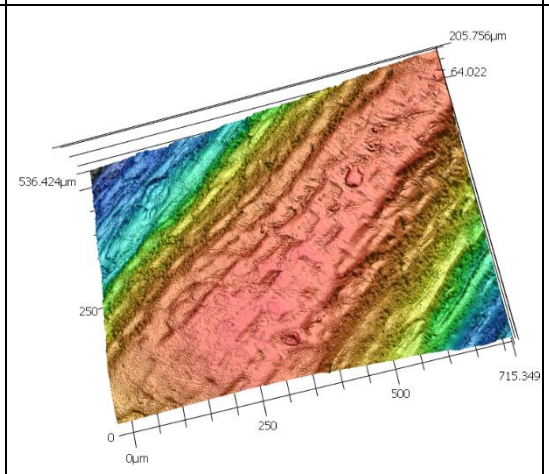	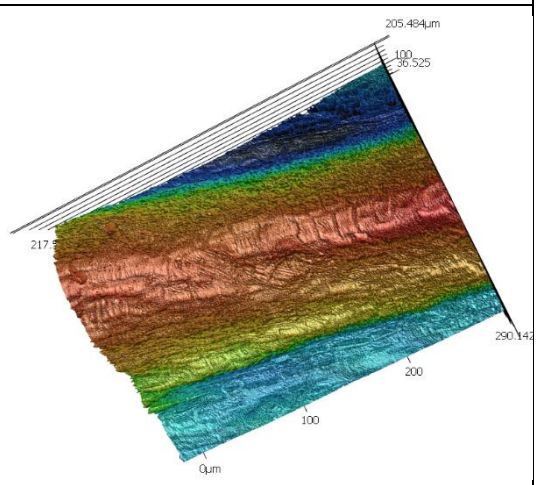
Pine-apple Lily	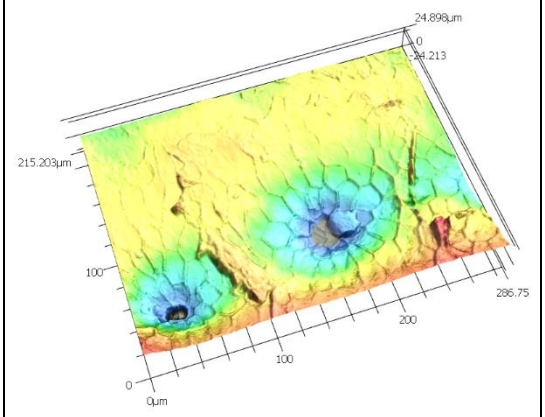	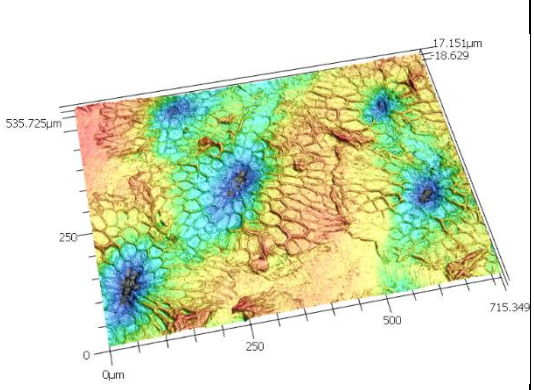
Elephant ear	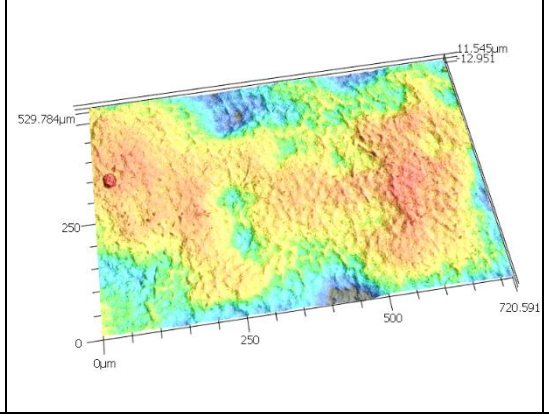	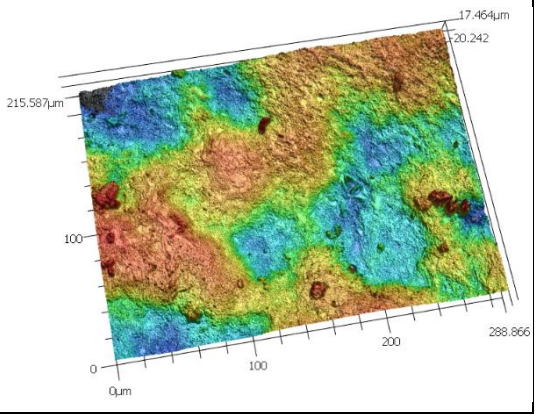

Reed-mace	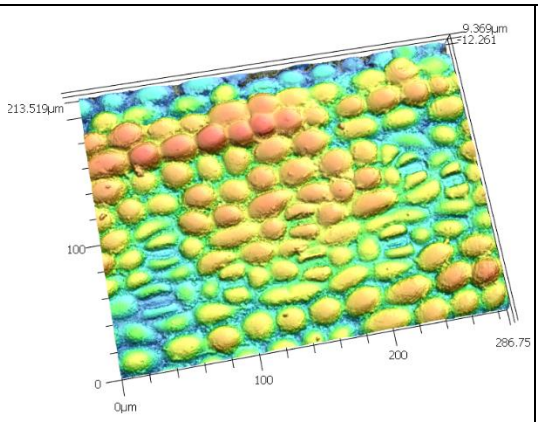	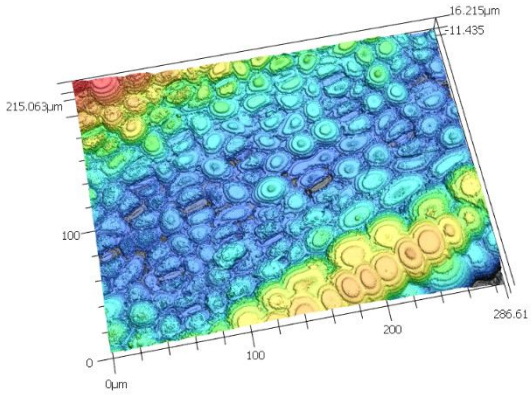
Sedum	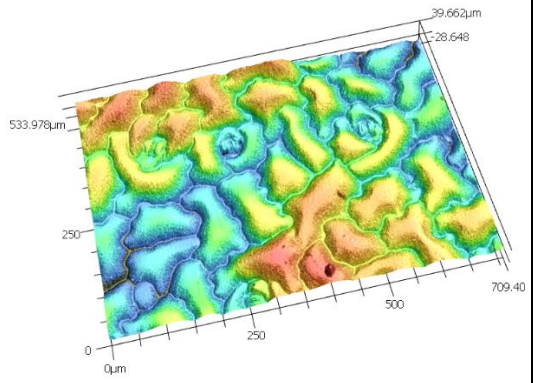	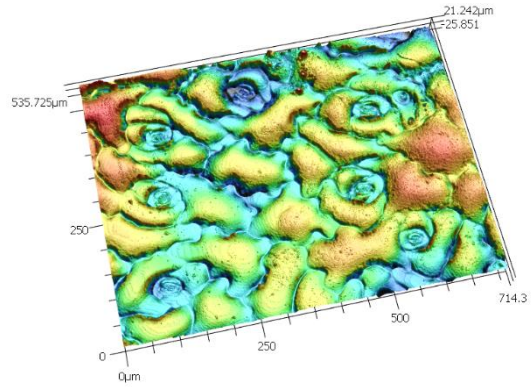
Onion	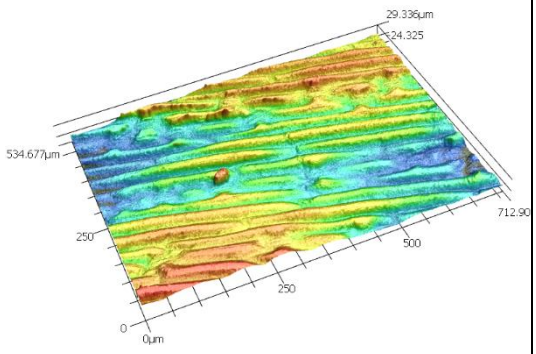	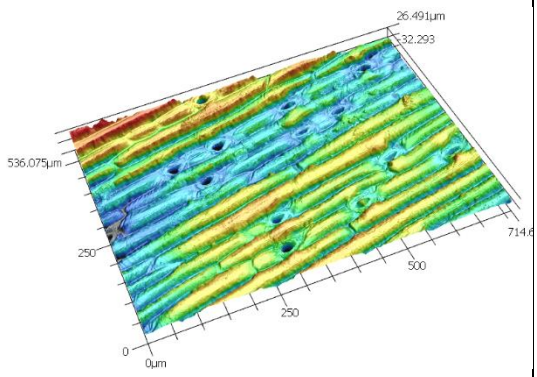
Holy Lotus	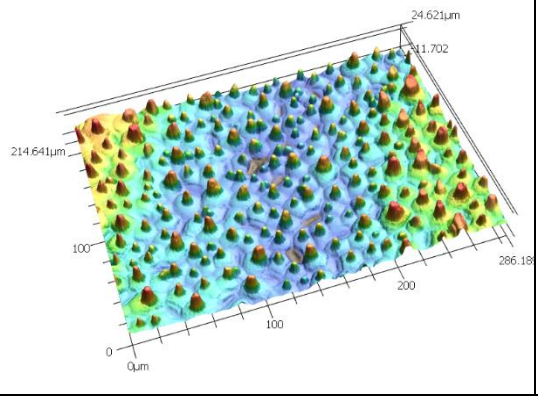	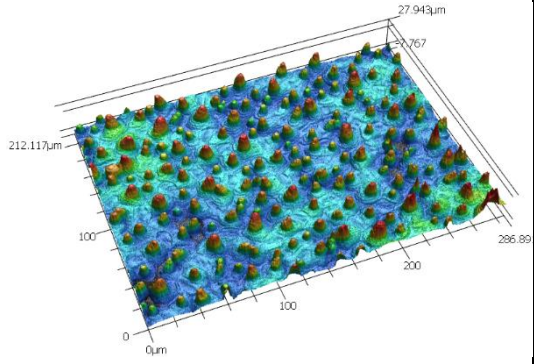

Rice	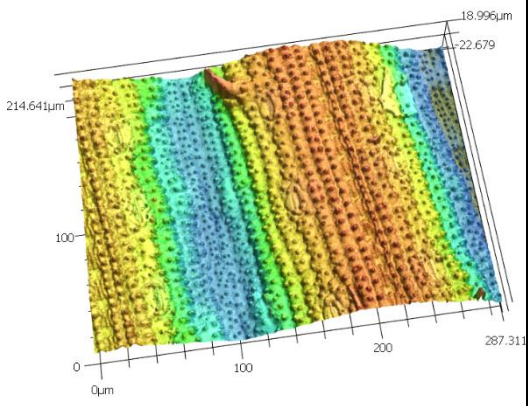	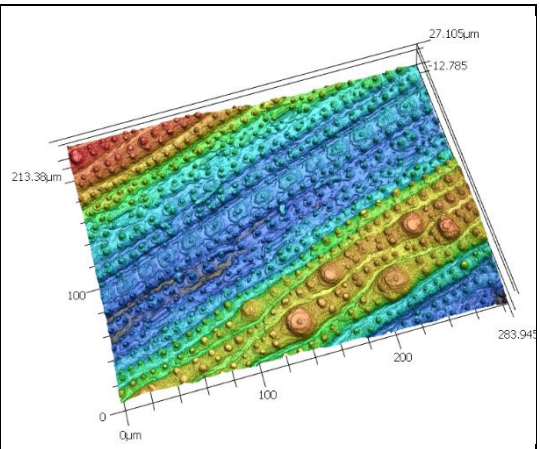
Plaintain Lily	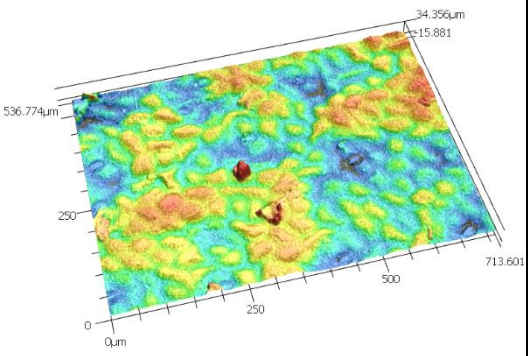	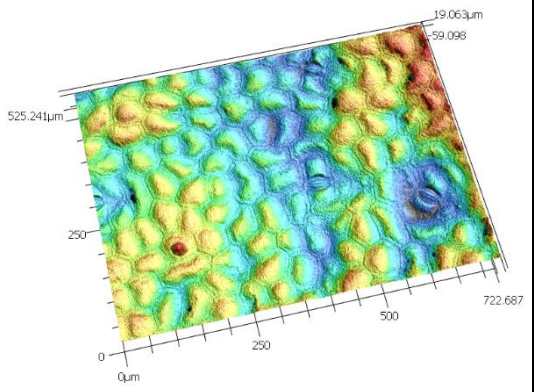
Hardy Canna	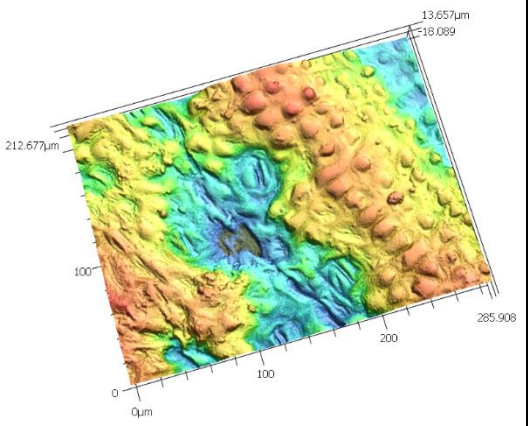	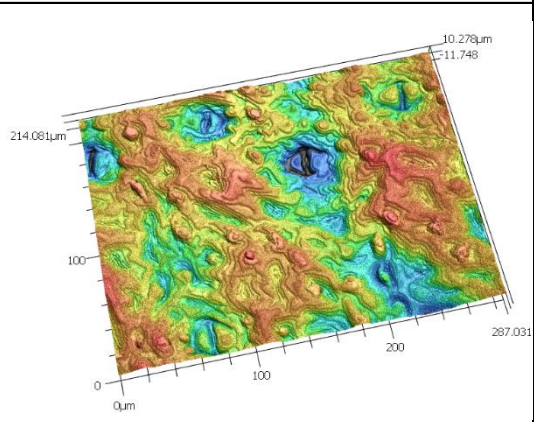
Venus flytrap	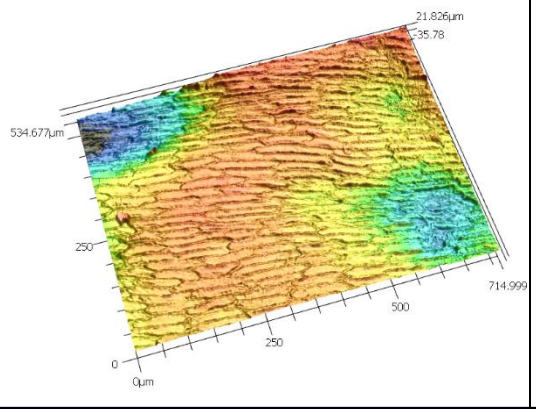	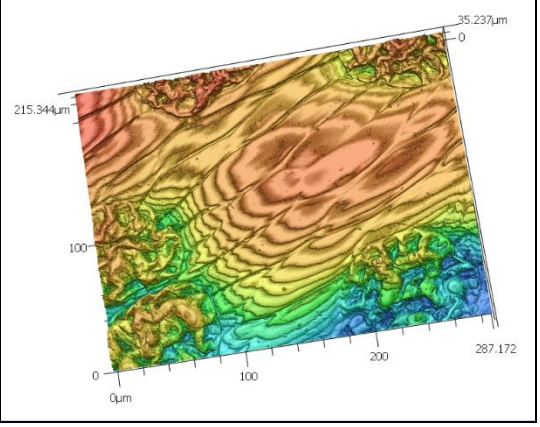

Supplementary Table 3. Contact angle measurements of the original and replica surfaces of superhydrophobic plants. Numbers between brackets represent the standard deviation of the population (n=3).

	Contact angle (°)	
	Original	Replica
Red Rose	127.2 (1.79)	129.6 (4.40)
Holy Lotus	140.5 (0.81)	135.2 (2.86)

Supplementary Table 4. Technical notes derived from the CellProfiler[64] 2.0 manual describing the metrics of the MeasureObjectSize module.

1. **Area:** The number of pixels in the region.
2. **Perimeter**: The total number of pixels around the boundary of each region in the image.
3. **FormFactor**: Calculated as $4*\pi*Area/Perimeter^2$. Equals 1 for a perfectly circular object.
4. **Solidity:** The proportion of the pixels in the convex hull that are also in the object, i.e., ObjectArea/ConvexHullArea.
5. **Extent:** The proportion of the pixels (2D) in the bounding box that are also in the region. Computed as the area/volume of the object divided by the area/volume of the bounding box.
6. **Center_X, Center_Y**: The x- and y- coordinates of the point farthest away from any object edge (the centroid).
7. **Eccentricity:** The eccentricity of the ellipse that has the same second-moments as the region. The eccentricity is the ratio of the distance between the foci of the ellipse and its major axis length. The value is between 0 and 1. (0 and 1 are degenerate cases; an ellipse whose eccentricity is 0 is actually a circle, while an ellipse whose eccentricity is 1 is a line segment.)

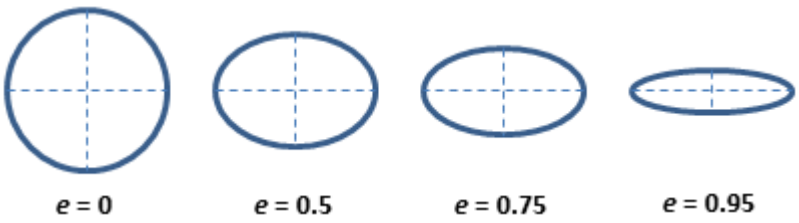

8. **MajorAxisLength:** The length (in pixels) of the major axis of the ellipse that has the same normalized second central moments as the region.
9. **MinorAxisLength:** The length (in pixels) of the minor axis of the ellipse that has the same normalized second central moments as the region.
10. **Orientation:** The angle (in degrees ranging from -90 to 90 degrees) between the x-axis and the major axis of the ellipse that has the same second-moments as the region.
11. **Compactness:** The mean squared distance of the object's pixels from the centroid divided by the area. A filled circle will have a compactness of 1, with irregular objects or objects with holes having a value greater than 1.
12. **MaximumRadius**: The maximum distance of any pixel in the object to the closest pixel outside of the object. For skinny objects, this is 1/2 of the maximum width of the object.
13. **MedianRadius:** The median distance of any pixel in the object to the closest pixel outside of the object.
14. **MeanRadius:** The mean distance of any pixel in the object to the closest pixel outside of the object.
15. **MinFeretDiameter, MaxFeretDiameter:** The Feret diameter is the distance between two parallel lines tangent on either side of the object (imagine taking a caliper and measuring the object at various angles). The minimum and maximum Feret diameters are the smallest and largest possible diameters, rotating the calipers along all possible angles.

References

1. Mahla, R. S. Stem cells applications in regenerative medicine and disease therapeutics. *Int. J. Cell Biol.* **2016,** (2016).

2. Thomson, J. A. *et al.* Embryonic Stem Cell Lines Derived from Human Blastocysts. **1145,** 1145–1148 (2008).

3. Ullah, I., Subbarao, R. B. & Rho, G. J. Human mesenchymal stem cells - current trends and future prospective. *Biosci. Rep.* **35,** 1–18 (2015).

4. Mao, A. S. & Mooney, D. J. Regenerative medicine: Current therapies and future directions. *Proc. Natl. Acad. Sci.* **112,** 14452–14459 (2015).

5. Schuldiner, M., Yanuka, O., Itskovitz-Eldor, J., Melton, D. A. & Benvenisty, N. Effects of eight growth factors on the differentiation of cells derived from human embryonic stem cells. *Proc. Natl. Acad. Sci. U. S. A.* **97,** 11307–12 (2000).

6. Murphy, W. L., McDevitt, T. C. & Engler, A. J. Materials as stem cell regulators. *Nat. Mater.* **13,** 547–557 (2014).

7. Marklein, R. A. & Burdick, J. A. Controlling stem cell fate with material design. *Adv. Mater.* **22,** 175–189 (2010).

8. Park, J. *et al.* TiO2 nanotube surfaces: 15 nm - an optimal length scale of surface topography for cell adhesion and differentiation. *Small* **5,** 666–671 (2009).

9. McBeath, R., Pirone, D. M., Nelson, C. M., Bhadriraju, K. & Chen, C. S. Cell shape, cytoskeletal tension, and RhoA regulate stemm cell lineage commitment. *Dev. Cell* **6,** 483–495 (2004).

10. Dalby, M. J. *et al.* The control of human mesenchymal cell differentiation using nanoscale symmetry and disorder. *Nat. Mater.* **6,** 997–1003 (2007).

11. Unadkat, H. V. *et al.* An algorithm-based topographical biomaterials library to instruct cell fate. *Proc. Natl. Acad. Sci.* **108,** 16565–16570 (2011).

12. Lovmand, J. *et al.* The use of combinatorial topographical libraries for the screening of enhanced osteogenic expression and mineralization. *Biomaterials* **30,** 2015–2022 (2008).

13. Moe, A. A. K. *et al.* Microarray with micro- and nano-topographies enables identification of the optimal topography for directing the differentiation of primary murine neural progenitor cells. *Small* **8,** 3050–3061 (2012).

14. Reimer, A. *et al.* Scalable topographies to support proliferation and Oct4 expression by human induced pluripotent stem cells. *Sci. Rep.* **6,** 18948 (2016).

15. Kolind, K. *et al.* A combinatorial screening of human fibroblast responses on micro-structured surfaces. *Biomaterials* **31,** 9182–9191 (2010).

16. Tan, K. K. B. *et al.* Enhanced differentiation of neural progenitor cells into neurons of the mesencephalic dopaminergic subtype on topographical patterns. *Biomaterials* **43,** 32–43 (2015).

17. Huang, Q. *et al.* Effects of hierarchical micro/nano-topographies on the morphology, proliferation and differentiation of osteoblast-like cells. *Colloids Surfaces B Biointerfaces* **145,** 37–45 (2016).

18. Shen, X. *et al.* Mesenchymal stem cell growth behavior on micro/nano hierarchical surfaces of

titanium substrates. *Colloids Surfaces B Biointerfaces* **127,** 221–232 (2015).

19. Kunzler, T. P., Drobek, T., Schuler, M. & Spencer, N. D. Systematic study of osteoblast and fibroblast response to roughness by means of surface-morphology gradients. *Biomaterials* **28,** 2175–2182 (2007).

20. Anselme, K. *et al.* Qualitative and quantitative study of human osteoblast adhesion on materials with various surface roughnesses. *J. Biomed. Mater. Res.* **49,** 155–166 (2000).

21. Faia-torres, A. B. *et al.* Differential regulation of osteogenic differentiation of stem cells on surface roughness gradients. *Biomaterials* **35,** 9023–9032 (2014).

22. Ivanova, E. P. *et al.* Natural bactericidal surfaces: Mechanical rupture of pseudomonas aeruginosa cells by cicada wings. *Small* **8,** 2489–2494 (2012).

23. Barthlott, W. & Neinhuis, C. Purity of the sacred lotus, or escape from contamination in biological surfaces. *Planta* **202,** 1–8 (1997).

24. Dean, B. & Bhushan, B. Shark-skin surfaces for fluid-drag reduction in turbulent flow: a review. *Philos. Trans. R. Soc. A Math. Phys. Eng. Sci.* **368,** 5737–5737 (2010).

25. Koch, K., Bhushan, B. & Barthlott, W. Multifunctional surface structures of plants: An inspiration for biomimetics. *Prog. Mater. Sci.* **54,** 137–178 (2009).

26. Wootton, R. J. Functional morphology of insect wings. (1992).

27. Alakpa, E. V. *et al.* Nacre Topography Produces Higher Crystallinity in Bone than Chemically Induced Osteogenesis. *ACS Nano* **11,** 6717–6727 (2017).

28. Diu, T. *et al.* Cicada-inspired cell-instructive nanopatterned arrays. *Sci. Rep.* **4,** (2014).

29. Mao, C. *et al.* Preparation of lotus-leaf-like polystyrene micro- and nanostructure films and its blood compatibility. *J. Mater. Chem.* **19,** 9025 (2009).

30. Goral, V. N., Hsieh, Y.-C., Petzold, O. N., Faris, R. A. & Yuen, P. K. Hot embossing of plastic microfluidic devices using poly (dimethylsiloxane) molds. *14th Int. Conf. Miniaturized Syst. Chem. Life Sci.* 1214–1216 (2010). doi:10.1088/0960-1317/21/1/017002

31. Ensikat, H. J., Boese, M., Mader, W., Barthlott, W. & Koch, K. Crystallinity of plant epicuticular waxes: electron and X-ray diffraction studies. *Chem. Phys. Lipids* **144,** 45–59 (2006).

32. Bray, M. A. *et al.* Cell Painting, a high-content image-based assay for morphological profiling using multiplexed fluorescent dyes. *Nat. Protoc.* **11,** 1757–1774 (2016).

33. Schindelin, J. *et al.* Fiji: An open-source platform for biological-image analysis. *Nat. Methods* **9,** 676–682 (2012).

34. R Core Team. R: A language and environment for statis- tical computing. (2009).

35. Ivanova, E. P. *et al.* Bactericidal activity of black silicon. *Nat. Commun.* **4,** 1–7 (2013).

36. A Kassambara, F. M. Factoextra: extract and visualize the results of multivariate data analyses. (2016).

37. Lecuit, T. & Lenne, P. F. Cell surface mechanics and the control of cell shape, tissue patterns and morphogenesis. *Nat. Rev. Mol. Cell Biol.* **8,** 633–644 (2007).

38. Kilian, K. A., Bugarija, B., Lahn, B. T. & Mrksich, M. Geometric cues for directing the differentiation of mesenchymal stem cells. *Proc. Natl. Acad. Sci.* **107,** 4872–4877 (2010).

39. Lü, D., Luo, C., Zhang, C., Li, Z. & Long, M. Differential regulation of morphology and stemness of mouse embryonic stem cells by substrate stiffness and topography. *Biomaterials* **35,** 3945–3955 (2014).

40. Seo, C. H., Furukawa, K., Montagne, K., Jeong, H. & Ushida, T. The effect of substrate microtopography on focal adhesion maturation and actin organization via the RhoA/ROCK pathway. *Biomaterials* **32,** 9568–9575 (2011).

41. Chen, C. S., Alonso, J. L., Ostuni, E., Whitesides, G. M. & Ingber, D. E. Cell shape provides global control of focal adhesion assembly. *Biochem. Biophys. Res. Commun.* **307,** 355–361 (2003).

42. Lim, J. Y. *et al.* The regulation of integrin-mediated osteoblast focal adhesion and focal adhesion kinase expression by nanoscale topography. *Biomaterials* **28,** 1787–1797 (2007).

43. Kalkan, T. *et al.* Tracking the embryonic stem cell transition from ground state pluripotency. *Development* **144,** 1221–1234 (2017).

44. Amit, M. & Itskovitz-eldor, J. Embryonic Stem Cells : Isolation , Characterization and Culture. *Adv Biochem Engin/Biotechnol* 173–184 (2009). doi:10.1007/10

45. Jaggy, M. *et al.* Hierarchical Micro-Nano Surface Topography Promotes Long-Term Maintenance of Undifferentiated Mouse Embryonic Stem Cells. *Nano Lett.* **15,** 7146–7154 (2015).

46. Ankam, S. *et al.* Substrate topography and size determine the fate of human embryonic stem cells to neuronal or glial lineage. *Acta Biomater.* **9,** 4535–4545 (2013).

47. Ghanian, M. H. *et al.* Nanotopographical control of human embryonic stem cell differentiation into definitive endoderm. *J. Biomed. Mater. Res. - Part A* **103,** 3539–3553 (2015).

48. Smus, J. P. *et al.* Tracking adipogenic differentiation of skeletal stem cells by label-free chemically selective imaging. *Chem. Sci.* **6,** 7089–7096 (2015).

49. Wang, P. Y., Li, W. T., Yu, J. & Tsai, W. B. Modulation of osteogenic, adipogenic and myogenic differentiation of mesenchymal stem cells by submicron grooved topography. *J. Mater. Sci. Mater. Med.* **23,** 3015–3028 (2012).

50. Abagnale, G. *et al.* Surface topography enhances differentiation of mesenchymal stem cells towards osteogenic and adipogenic lineages. *Biomaterials* **61,** 316–326 (2015).

51. Keselowsky, B. G., Collard, D. M. & García, A. J. Integrin binding specificity regulates biomaterial surface chemistry effects on cell differentiation. *Proc. Natl. Acad. Sci. U. S. A.* **102,** 5953–5957 (2005).

52. Davidson, P. M., Özçelik, H., Hasirci, V., Reiter, G. & Anselme, K. Microstructured surfaces cause severe but non-detrimental deformation of the cell nucleus. *Adv. Mater.* **21,** 3586–3590 (2009).

53. Koch, B. *et al.* Confinement and Deformation of Single Cells and Their Nuclei Inside Size-Adapted Microtubes. *Adv. Healthc. Mater.* **3,** 1753–1758 (2014).

54. Yang, K. *et al.* Electroconductive Nanoscale Topography for Enhanced Neuronal Differentiation and Electrophysiological Maturation of Human Neural Stem Cells. *Nanoscale* 18737–18752 (2017). doi:10.1039/C7NR05446G

55. Rasmussen, C. H. *et al.* Enhanced Differentiation of Human Embryonic Stem Cells Toward

Definitive Endoderm on Ultrahigh Aspect Ratio Nanopillars. *Adv. Funct. Mater.* **26,** 815–823 (2016).

56. Jeon, K. *et al.* Self-renewal of embryonic stem cells through culture on nanopattern polydimethylsiloxane substrate. *Biomaterials* **33,** 5206–5220 (2012).

57. Bauwens, C. L. *et al.* Control of Human Embryonic Stem Cell Colony and Aggregate Size Heterogeneity Influences Differentiation Trajectories. *Stem Cells* **26,** 2300–2310 (2008).

58. Joshi, R., Buchanan, J. & Tavana, H. Colony size effect on neural differentiation of embryonic stem cells microprinted on stromal cells. *2016 38th Annu. Int. Conf. IEEE Eng. Med. Biol. Soc.* 4173–4176 (2016). doi:10.1109/EMBC.2016.7591646

59. Murray, P. *et al.* The self-renewal of mouse embryonic stem cells is regulated by cell-substratum adhesion and cell spreading. *Int. J. Biochem. Cell Biol.* **45,** 2698–2705 (2013).

60. McMurray, R. J. *et al.* Nanoscale surfaces for the long-term maintenance of mesenchymal stem cell phenotype and multipotency. *Nat. Mater.* **10,** 637–644 (2011).

61. von der Mark, K., Bauer, S., Park, J. & Schmuki, P. Another look at 'Stem cell fate dictated solely by altered nanotube dimension'. *Proc. Natl. Acad. Sci.* **106,** E60–E60 (2009).

62. Kingham, E., White, K., Gadegaard, N., Dalby, M. J. & Oreffo, R. O. C. Nanotopographical Cues Augment Mesenchymal Differentaition of Human Embryonic Stem Cells. 2140–2151 (2013). doi:10.1002/smll.201202340

63. Bach Q. Le *et al.* Micro-Topographies Promote Late Chondrogenic Differentiation Markers in the ATDC5 Cell Line. *Tissue Eng. Part A* **23,** 458–469 (2017).

64. Carpenter, A. E. *et al.* CellProfiler: Image analysis software for identifying and quantifying cell phenotypes. *Genome Biol.* **7,** (2006).